

## THE INSIGNIFICANCE OF GLOBAL REHEATING IN THE ABELL 1068 CLUSTER: X-RAY ANALYSIS

MICHAEL W. WISE<sup>1</sup>, BRIAN R. MCNAMARA<sup>2</sup>, AND STEVE S. MURRAY<sup>3</sup>

Massachusetts Institute of Technology, Center for Space Research  
Building NE80-6007, Cambridge, MA 02139-4307  
wise@space.mit.edu

To appear in the January 10, 2004 issue of the *Astrophysical Journal*

### ABSTRACT

We report on a *Chandra* observation of the massive, medium redshift ( $z = 0.1386$ ) cooling flow cluster Abell 1068. We detect a clear temperature gradient in the X-ray emitting gas from  $kT \sim 5$  keV in the outer part of the cluster down to roughly 2 keV in the core, and a striking increase in the metallicity of the gas toward the cluster center. The total spectrum from the cluster can be fit by a cooling flow model with a total mass deposition rate of  $\sim 150 M_{\odot} \text{ yr}^{-1}$ . Within the core ( $r < 30$  kpc), the mass deposition rate of  $\sim 40 M_{\odot} \text{ yr}^{-1}$  is comparable to estimates for the star formation rate from optical data. We find an apparent correlation between the cD galaxy's optical isophotes and enhanced metallicity isocontours in the central  $\sim 100$  kpc of the cluster. We show that the approximate doubling of the metallicity associated with the cD can be plausibly explained by supernova explosions associated with the cD's ambient stellar population and the recent starburst. Finally, we calculate the amount of heating due to thermal conduction and show that this process is unlikely to offset cooling in Abell 1068.

*Subject headings:* cooling flows — galaxies: clusters: general — galaxies: elliptical and lenticular, cD — intergalactic medium — X-rays: galaxies

### 1. INTRODUCTION

Galaxy clusters frequently have high X-ray surface brightness cores due to thermal emission from dense gas. Absent a substantial and persistent heat source, this high density, relatively low temperature gas should cool on a timescale that is much less than the age of clusters, leading to a so-called “cooling flow” (Fabian 1994). The cooling rates reported from the low resolution X-ray observatories that operated throughout the previous two decades were often extraordinarily large, and frequently exceeded several hundred to over two thousand solar masses per year. Such large cooling rates posed a dilemma. They imply the presence of enormous sinks of cold gaseous and stellar matter in the cD galaxies found at the centers of cooling flows. Although substantial amounts of cold gas and vigorous star formation are now found commonly in cD galaxies centered in cooling flows (Edge 2001, Edge et al. 2002, Jaffe & Bremer 1997, Jaffe, Bremer, & Van der Werf 2001, Donahue et al. 2000, Falcke et al. 1998, Crawford et al. 1999, Cardiel, Gorgas, & Aragon-Salamanca 1998, McNamara & O’Connell 1989), they are found in quantities that are much smaller than these earlier cooling rates would imply (cf., McNamara 2002).

This large discrepancy between the cooling and star formation rates is one of the primary questions behind what has become known as the “cooling flow problem”. Simply stated, it is either a violation of mass continuity, assuming the matter is in fact not cooling at the rates implied by the X-ray data, or a missing light problem, if the matter is indeed cooling at these historically large rates but is hidden in some exotic state. Recent high spatial and spectral resolution cluster observations made with the *Chandra* and *XMM-Newton* X-ray observatories have changed this canonical dilemma and suggested a third possibility. The absence of detected emission lines from gas at temperatures less than about 3 keV in *XMM-Newton* RGS

and *Chandra* HETG observations of cluster cores implies that a large fraction of the cooling gas does not in fact cool below X-ray emitting temperatures (Peterson et al. 2001, Peterson et al. 2003, Wise et al. 2004). Instead, this gas is assumed to be reheated to ambient temperatures by one or more of several possible agents that are now being extensively studied. These agents include mechanical and cosmic ray reheating from supernova explosions, heat conduction from the hot outer layers of clusters, and mechanical heating by the central radio sources in cD galaxies.

Images of the cooling flow regions of clusters now show a great deal of structure, including the large cavities or bubbles in the X-ray emission associated with the radio sources harbored by the central cluster galaxies (e.g., McNamara et al. 2000, Fabian et al. 2000). The strong interactions between the radio sources generated in the nuclei of cD galaxies and the surrounding X-ray emitting gas may reduce the cooling rates and bring them more in line with the star formation rates (David et al. 2001, Nulsen et al. 2002). In addition, *Chandra*'s superb spatial resolution provides the capability to map the temperature structure of the keV gas on fine spatial scales, which permits a direct comparison between the sites of star formation seen at optical and ultraviolet wavelengths, and sites of rapid cooling. In essence, we can now reevaluate the proposition that cooling flows are fueling star formation by comparing the cooling and star formation rates on the same spatial scales. In addition, the newly revealed complexity of the gas in cluster cores has sparked a reevaluation of several possible heating mechanisms, such as AGN heating (Brighenti & Mathews 2002, Ruszkowski & Begelman 2002), heat conduction from the hotter outer layers of clusters (Narayan & Medvedev 2001, Zakamska & Narayan 2003), and supernovae.

In this paper, we present a detailed examination of the X-ray structure of the core of the Abell 1068 galaxy, and present

<sup>1</sup> Massachusetts Institute of Technology, Center for Space Research, Cambridge, MA 02139-4307

<sup>2</sup> Dept. of Physics & Astronomy, Ohio University, Athens, OH, 45701

<sup>3</sup> Harvard-Smithsonian Center for Astrophysics, MS 70, 60 Garden Street, Cambridge, MA 02138

some of the most detailed temperature, and metallicity maps available for a galaxy cluster. In a companion paper (McNamara, Wise, & Murray 2004, hereafter “Paper 2”), we discuss the remarkable starburst properties of the Abell 1068 cD galaxy and present a detailed comparison between the X-ray and optical properties of the cD. In these papers, we show that 90% of the ultraviolet light from the starburst is emerging from the region of the cluster with the shortest cooling time, and that the star formation rates and local cooling rates agree. However, we stop short of presenting this fact as proof that the starburst is being fueled by the cooling flow, as there are independent data to suggest that the starburst may be associated with an ongoing dynamical interaction between the cD and a group of companion galaxies. In the proceeding analysis, we have adopted a redshift for Abell 1068 of  $z = 0.1386$  (Crawford et al. 1999) and a cosmology with  $H_0 = 70 \text{ km s}^{-1} \text{ Mpc}^{-1}$ ,  $\Omega_M = 0.3$ , and  $\Omega_\Lambda = 0.7$ . These assumptions yield a luminosity distance of  $D = 645 \text{ Mpc}$ , an angular diameter distance of  $505 \text{ Mpc}$ , and a linear scale of  $2.45 \text{ kpc per arcsec}$ .

## 2. OBSERVATIONS AND DATA REDUCTION

Abell 1068 was observed by *Chandra* on Feb. 4, 2001 for 30 ksec using the ACIS-S3 back-illuminated CCD (OBSID 01652). After standard filtering, the net exposure time was 26.8 ksec. The data were examined for evidence of bad aspect correction and background flares but were found to be free of both defects. Standard level 2 event files were created using the latest ACIS calibration products appropriate for the observed focal plane temperature of  $-120^\circ \text{ C}$ . All data preparation and creation of analysis products (exposure maps, response matrices, etc.) employed the CIAO 2.2.1 data analysis tools and version 2.9 of the *Chandra* calibration database.

The X-ray morphology of Abell 1068 is complex exhibiting a highly elliptical appearance on larger scales ( $\sim 300\text{--}400 \text{ kpc}$ ) and complicated structure in the core ( $r \lesssim 50 \text{ kpc}$ ). This morphology is illustrated in Figure 1 which shows an exposure corrected, adaptively smoothed flux image of Abell 1068 in the  $0.3\text{--}7.0 \text{ keV}$  band. The X-ray emission exhibits a strong central peak centered on the central galaxy characteristic of “cooling flow” clusters. The exact location of the X-ray peak was determined by fitting a two dimensional, elliptical Lorentzian surface with varying minor over major axis ratio and position angle. The resulting centroid position was  $(10 \ 40 \ 44.5, +39 \ 57 \ 12.3)$  which is within  $1.95 \text{ arcsec}$  of the optical position of the central cD galaxy  $(10 \ 40 \ 44.62 +39 \ 57 \ 10.2)$ . The best fit values for the position angle and axis ratio were  $\theta = 133^\circ \pm 3^\circ$  and  $\epsilon = 0.71 \pm 0.02$ , respectively. These values were used in all subsequent spatial and spectral analyses.

A number of bright point sources are evident in the field of Abell 1068 including a bright source  $\sim 23 \text{ arcsec}$  south associated with the radio source B3 1037+401. Although these sources contribute a very small fraction of the detected events in the field (typically  $\sim 100\text{--}400 \text{ counts each}$ ), we have excluded them prior to extracting the spectral and surface brightness information presented here. The CIAO tool `WAVDETECT` was used to determine positions and sizes for point sources in the field. These sources were then excised from the event file for all further analysis.

All spectral analysis was done using the ISIS (Houck & DeNicola 2000) spectral fitting package which includes the standard XSPEC (Arnaud 1996) model library as well as access to the high resolution APED database

(Smith et al. 2001). ACIS effective area files (ARFs) and response matrices (RMFs) were computed using the standard CIAO tools and calibration files. A correction for the time-dependent degradation of the ACIS effective area due to contamination buildup on the optical blocking filter was also included. All analysis was conducted using the gain-corrected, PI data. A single RMF was computed appropriate for the centroid position of Abell 1068. Variations in the resolution of the CCD, as captured in the response matrices, over the region encompassing Abell 1068 were found to be small ( $\lesssim 10\%$ ). Fits using RMFs computed at other positions in the cluster as well as counts-weighted, average RMFs gave equivalent results within the errors. Effective area files were calculated at individual positions as appropriate. Finally, background files for the spectral analysis were extracted from the edge of the ACIS-S3 CCD, far outside the largest extracted cluster region.

## 3. SPECTRAL ANALYSIS

In order to study the spectral character of the X-ray emission from Abell 1068, we have performed three distinct analyses. First, an integrated spectrum comprising the majority of the emission from the cluster was extracted to examine global properties such as mean temperature, abundance, and total X-ray cooling rate if appropriate. We have also performed a spatially resolved analysis using spectra extracted in elliptical annuli to study global trends in the temperature, abundance, and mass deposition profile as a function of radius in the cluster. Finally, we have performed a fully two-dimensional mapping of various spectral parameters in the core of Abell 1068 to compare the complicated X-ray spatial structure with observed structures in other wavebands. We discuss each of these analyses and their results here in turn.

### 3.1. Integrated Spectrum

Extracting a “total” spectrum for Abell 1068 is complicated by the fact that the cluster spans more than one ACIS CCD. While variations in the resolution from different locations on the chip are typically small for the S3 aimpoint CCD (where the majority of the emission from Abell 1068 is located), they can be quite sizable (factors of  $\sim 2\text{--}4$  depending on energy) on front-illuminated (FI) CCDs. This difference makes combining spectra from ACIS-S3 with spectra from neighboring FI chips impractical. Consequently, we have restricted our integrated spectral analysis to only that emission contained on ACIS-S3. A  $175 \times 129 \text{ arcsec}$  elliptical extraction region centered on the X-ray peak and oriented with the measured position angle was used (see §2). This region corresponds to a linear extent of  $0.576 \text{ Mpc}$  (as measured along the semi-major axis) and comprises  $\sim 77\%$  of the total cluster flux as determined from the surface brightness analysis discussed below in §4. The resulting spectrum contained 65634 counts after background subtraction and was adaptively binned to yield a minimum of 30 counts per bin prior to analysis.

We have considered five types of models in fitting the integrated spectrum from Abell 1068. In the simplest of these, the X-ray emission was represented by a single isothermal plasma (hereafter denoted 1T) using the MEKAL model from the XSPEC library in ISIS where the temperature and elemental abundance were allowed to vary. As an intermediate case between a single temperature plasma and a fully multi-phase model, we also considered a model with two temperature components (2T subsequently). In addition, three models were em-

ployed consisting of a single temperature MEKAL model plus a multi-phase cooling flow component (MKCFLOW in ISIS). For all models featuring a cooling flow, the ambient temperature of the MEKAL component and the upper bound on the cooling gas were tied. In models with multiple components, the abundances were tied together and allowed to vary. A foreground Galactic absorption column was included in all five models and each model was fit twice: once allowing the foreground Galactic absorption column to vary, and then a second time fixing the column to the canonical value of  $1.40 \times 10^{20} \text{ cm}^{-2}$ .

The lower bound on the gas temperature in the cooling flow models was chosen to reflect differing scenarios for the fate of the cooling material. A scenario where the gas was assumed to fully cool below X-ray emitting temperatures was modeled by fixing the lower temperature bound at 0.1 keV. We have denoted this model as FC (full cooling). However, recent XMM RGS and *Chandra* HETG observations of cluster cores have failed to detect emission lines from gas at temperatures less than about 3 keV indicating that cooling may be truncated somehow (Peterson et al. 2001, Peterson et al. 2003, Wise et al. 2004). This situation was replicated by fixing the lower temperature bound of the cooling flow component to a value of 2 keV, consistent with the observed radial temperature profile discussed in §3.2, and has been denoted TC (truncated cooling). Finally, a model where the lower limit on the temperature of the cooling gas was allowed to be a free parameter was considered (hereafter denoted VC for variable cooling).

The resulting spectral parameters for all 10 models are presented in Table 1. As a general comment, all models do a reasonable job at fitting the integrated spectrum, especially at energies above 1.0 keV, yielding reduced  $\chi^2$  values ranging from 1.1–1.3. Differences in the fits are driven by the spectrum below 1.0 keV. Models with freely varying absorption do a better job than models with the canonical value. Derived columns are typically 70% higher than the reported value. This difference could be related to ACIS calibration uncertainties below 1.0 keV. Alternatively, it could represent the presence of excess absorption associated with the cooling material or other cold gas in the core though this interpretation seems unlikely (see §3.2). The single temperature component (1T) fits indicate a global, mean gas temperature of  $\sim 4$  keV and a metallicity of 0.5 solar abundance. The spectral data, however, clearly indicate the presence of multiple temperature components. This result is not surprising given the clear temperature gradient in the spatially resolved analysis. Formally, the best fit is achieved by the 2T model with temperature components of  $T_1 \sim 7.0$  keV and  $T_2 \sim 2.0$  keV and a reduced  $\chi^2 = 1.1$ . These derived temperatures are not particularly sensitive to the value of the absorbing column. However, this fit results in systematic residuals below 0.7 keV. The cooling flow models give equivalent values of  $\chi^2$  and better residuals at low energies.

With CCD resolution spectra alone, it can be difficult to distinguish between various cooling flow models. For Abell 1068, we find that the full cooling (FC) model with free Galactic absorption produces the lowest  $\chi^2$  value and most uniformly distributed residuals below 1.0 keV. Figure 2 shows the best fit FC model overlaid on the data. The resulting cooling rate for the FC model was determined to be  $\dot{M}_X \sim 115\text{--}150 M_\odot \text{ yr}^{-1}$  with an ambient gas temperature consistent with the global mean. This rate drops to  $\sim 40 M_\odot \text{ yr}^{-1}$  if the standard Galactic column is used. If the cooling is truncated at 2.0 keV, then the resulting deposition rates are increased dramatically reaching

values of  $\dot{M}_X \sim 900\text{--}1000 M_\odot \text{ yr}^{-1}$ . Such an increase is to be expected of course, since if the gas cools over a smaller temperature range, then more gas must cool in order to produce the same flux as in the FC model. Interestingly, the variable cooling models (VC) converge to a preferred lower temperature limit for the cooling gas of  $\sim 1.5$  keV with an accompanying small decrease in the cooling rate relative to the TC models. This value is consistent with the central temperature obtained from our deprojection analysis described below (see §3.3). However, the additional free parameters in this model render these fits somewhat unstable and make determining confidence limits difficult. So, while suggestive, one should view this result cautiously.

### 3.2. Annular Spectral Analysis

We have examined spatial variations in the physical state of the X-ray emitting plasma in Abell 1068 by dividing the elliptical region containing the previously discussed total spectrum into a series of concentric, elliptical annuli. The annuli were constructed to have the same axis ratio and orientation angle as before and were adaptively sized to include a minimum of 5000 counts after background subtraction. This requirement yielded 14 annuli out to a maximum, major-axis radius of 125 arcsec. The spectrum outside this radius is dominated by background emission. Spectra were extracted from each annular region and grouped in the same manner as the integrated spectrum. In all subsequent discussion, quoted radii shall refer to distances along the cluster's major-axis except where specifically noted.

In fitting the spectrum from each annuli, we considered the various models used to describe the total, integrated spectrum in Table 1. However, the lower signal to noise in the individual annular spectra make distinguishing between the various models difficult. As a general result, each of the annuli is well fit by a single temperature MEKAL plasma (the 1T model of Table 1) with  $\chi^2$  values ranging from 0.9–1.3. Additional temperature or cooling flow components do not produce significantly better fits. The exceptions to this rule are the central three annuli which show a slight improvement in fit quality when a second temperature component is included (2T models). Fits for these three annuli using the 2T models are consistent with cool gas at  $T \sim 2.0$  keV plus a contribution from hotter gas close to the global mean value of 4–5 keV. As we discuss in §3.3, the presence of these two components is consistent with projection effects due to hotter gas along the line of sight. Such contamination is more easily resolved in the central annuli due to the larger temperature difference between the intrinsic cool, core gas and the outer, hotter cluster gas.

There is a clear temperature gradient from 5.5 keV in the outer parts of the cluster down to  $\sim 2.5$  keV in the core (see Figure 3). The temperature drops steadily in to a radius of  $\sim 20$  kpc ( $\sim 8$  arcsec) and then flattens although only two bins cover this region. The innermost annulus shows a slight temperature increase which may be due to emission from either a central AGN or the observed starburst in Abell 1068. Fits to this central annulus including a power-law component to represent emission from a central AGN do not however result in a better fit nor do they constrain the hardness of the suspected AGN emission. For an assumed photon index of 1, we can place an upper limit of  $5.3 \times 10^{-13} \text{ ergs s}^{-1} \text{ cm}^{-2}$  on the unabsorbed, 0.3–10.0 keV flux from any central AGN. This limit represents a maximum of  $\sim 40\%$  of the flux from within the central  $\sim 4$  arcsecs. If a photon index of 2 is assumed, this limits rises to 45%. Given

these upper limits, the observed temperature increase in the innermost annulus is more likely to be associated with energy injection from the starburst.

The abundance in the gas shows a steady increase toward the center of the cluster from a value of  $\sim 0.2$  solar at the outer edge to a central value of  $\sim 1.0$  solar (see Figure 4). There is no evidence for a radial dependence on the amount of absorbing column in the cluster. At all radii, the measured column is consistent with the values obtained from fits to the global spectrum with free absorption (see Figure 5). This result would argue against the presence of intrinsic, excess absorption associated with accumulated cooled gas from a cooling flow. Even if ACIS calibration uncertainties make the absolute magnitude of the fitted absorbing column suspect, one would expect a relative increase toward the center of the cluster if excess absorption associated with the cooling gas were present.

Finally, we have measured the mass deposition rate assuming a cooling flow model. In contrast to the annular analysis, the cooling flow models were fit to concentric elliptical extraction regions of increasing radius. Therefore, the measured value of  $\dot{M}_X(< r)$  corresponds to the total cooling rate within a given radius. Both the TC and FC models were fit and show similar a radial dependence qualitatively. Of the two cooling models, the FC model gives marginally better fits although, again, the quality of the data does not allow a definitive selection between the two options. The lower signal to noise of the resolved spectra precluded fitting the VC model. Figure 6 shows the resulting profile for the FC model. In the core region ( $r \lesssim 25$  kpc), we find a value of  $\dot{M}_X(< r) \sim 40 M_\odot \text{ yr}^{-1}$ . As we discuss in Paper II, this value is consistent with the rates of massive star formation implied by optical data in Abell 1068.  $\dot{M}_X$  increases steadily with radius reaching a maximum value of  $\sim 150 M_\odot \text{ yr}^{-1}$  in the outer parts of the cluster. Fitting a functional form to the mass deposition profile of  $\dot{M}_X(< r) \propto r^\alpha$  yields a value of  $\alpha \sim 0.4$ , somewhat flatter than the  $M_X(< r) \propto r$  relation often seen in pre-*Chandra* cluster data.

### 3.3. Deprojected Temperature Profiles

Due to projection effects, the temperatures measured in the previous annular analysis actually represent the emission-weighted mean temperature of all gas along the line of sight within a given annulus. The spectrum extracted from a given elliptical annulus consists of a superposition of emission from the local volume bounded by the inner and outer ellipses and contributions from hotter gas at all larger radii. Consequently, in a standard analysis such as in §3.2, the measured gas temperature at a given radius will be higher than its actual local value. To correct for the effects of this projection, we have performed a spectral analysis on the same annular spectra used in the previous section accounting for the contribution of hotter gas at larger radii to the spectrum from any given annulus.

To calculate the contributions from gas along the line of sight, we have assumed the cluster to be composed of elliptical shells with boundaries given by the inner and outer radii of the annuli and an axis ratio fixed to the measured value. Since we have no information to constrain the inclination angle of the cluster, we have assumed the orientation to be perpendicular to the line of sight although the equations for the volume contributions are equivalent for the edge-on case. The intrinsic spectrum of each volume shell was modeled as a single MEKAL plasma with variable normalization, temperature, and elemental abundance and the fractional contribution of each volume

shell to the various annuli was then calculated. A foreground Galactic absorption component was included and allowed to vary. The spectra from all 14 annuli were then fit simultaneously to determine the intrinsic temperature profile in the cluster. This entire procedure has been implemented as a custom model within ISIS (Houck & DeNicola 2000) and is described in detail in Wise & Houck (2004). Similar techniques have been used by other groups to correct for projection in clusters such as Abell 2390 (Allen, Etti, & Fabian 2001) and Abell 2199 (Johnstone et al. 2002).

Qualitatively, the deprojected temperature profile is quite similar to that obtained from the standard annular analysis (see Figure 7), although with somewhat larger errors. At large radii, the temperature agrees with the simple analysis as one would expect since contamination from other shells drops with increasing radius. The biggest change occurs for the central temperature where we obtain a somewhat cooler minimum temperature of  $1.8 \pm 0.2$  keV as compared to the 2.5 keV obtained in the analysis of §3.2. As noted in the simple annular analysis, the innermost annulus remains somewhat hotter than the minimum temperature possibly due to contamination from an unresolved, central AGN. Values for the abundance were consistent with the simple annular analysis and the Galactic column was determined to be  $2.9 \times 10^{20} \text{ cm}^{-2}$ .

### 3.4. Temperature Map

It is apparent even by visual inspection that the X-ray emission from the core of Abell 1068 exhibits a complicated morphology (see Figure 1). As we discuss in more detail in Paper II, the optical data show similar complicated structures including condensed knots of extremely blue light presumably associated with sites of ongoing star formation (McNamara, Wise, & Murray 2004). In order to examine possible correlations between the plasma properties and features seen in other wavebands, we have constructed 2D maps of the gas temperature and abundance in Abell 1068. These maps were computed using a custom module within the ISIS (Houck & DeNicola 2000) spectral analysis package which automates the process of extracting spectra, generating appropriate ARFs and RMFs, and then fitting a given spectral model (see (Houck et al. 2004) for a detailed description).

The maps were generated using a grid of adaptively sized extraction regions selected to contain a minimum of 1000 counts in the 0.5–7.0 keV band. The grid was selected to span a  $300 \times 300$  arcsec region centered on Abell 1068. Due to the drop in surface brightness with increasing radius, the size of the extraction regions increases with radius. Consequently, sharp spatial features are not well resolved in the outer parts of the maps. In the core ( $r \lesssim 40$  kpc), however, the extraction regions range in size from  $\sim 2$ –10 arcsecs and features in the temperature or abundance distributions on these scales can be identified. Within each extraction region, the resulting spectrum was fit with a MEKAL plasma model including foreground Galactic absorption fixed at the nominal value of  $2.41 \times 10^{21} \text{ cm}^{-2}$  as determined from the integrated fits in §3.1. The plasma temperature and abundance were allowed to vary and single-parameter, 90% confidence limits were computed for both parameters at each map point. Typical errors for the measured temperatures and abundances range from 10%–30% over the map with the most accurate measurements corresponding to the central—most regions where the surface brightness is highest. Fits allowing the Galactic column to vary produced similar maps within the

measured uncertainties and in any event were morphologically equivalent.

The temperature map for the central  $80'' \times 80''$  of Abell 1068 is shown in Figure 8. The 0.3-7.0 keV X-ray surface brightness contours are overlaid for comparison. Although the overall temperature structure is consistent with the radial temperature profile presented in Figure 3, significant asymmetry in the gas temperature is apparent. To the southeast of the cD position, an arc of 2–3 keV is present. This extension of cooler gas is spatially coincident ( $r \sim 20$  arcsec) with several companion galaxies and may represent either gas associated with the ISM in these galaxies or stripped galactic gas from these companions. The region of coolest emission ( $T \sim 2.5$  keV) corresponds to the peak of the X-ray surface brightness profile and is offset from the optical centroid of the cD galaxy by  $\sim 2$  arcsec. However, this scale is comparable to the map resolution in the core and so may be consistent with a zero offset. As we discuss in Paper II, the sites of coolest X-ray emission in Abell 1068 correspond to over 90% of the emergent optical blue light from the starburst. We defer a detailed discussion of the implications for the star formation history in Abell 1068 to that work (McNamara, Wise, & Murray 2004).

In contrast, to the northwest, the temperature rises relatively steeply as one moves away from the central cD increasing from 2.5 keV to 5 keV within  $\sim 10$  arcsec ( $\sim 25$  kpc). This rapid rise in temperature corresponds to a sharp decline in the X-ray surface brightness at this position as seen in Figure 1. This position is also coincident with an inflection point in the azimuthally averaged surface brightness profile discussed in §4. Such temperature jumps and surface brightness discontinuities are characteristic of the “cold fronts” observed in many other clusters and may represent evidence for previous merger activity in Abell 1068 (Markevitch et al. 2000; Vikhlinin, Markevitch, & Murray 2001). We note however that the surface brightness inflection observed in Abell 1068 is much weaker than that typically seen in clusters featuring cold fronts such as Abell 2142 (Markevitch et al. 2000). We defer a more detailed analysis of this feature to a later work.

### 3.5. Abundance Map

The morphology of the abundance map in Abell 1068 is even more striking. Figure 9 shows the metallicity as determined from the MEKAL fits for the same  $80'' \times 80''$  central region. An optical image of the R-band light (F606W filter) in Abell 1068 was obtained from the HST archive and is overlaid for comparison. There is a clear pattern of enrichment extending along the semi-major axis of the cluster and the central cD galaxy. Several filamentary extensions of roughly solar metallicity gas are also apparent and in all cases extend from the center to the position of the various companion galaxies in the cluster. Since the map abundances are measured in projection, local abundances may be somewhat higher.

Several researchers have found a trend between increasing metal abundance and the presence of a cD galaxy in the central regions of clusters (Fukazawa et al. 2000, Irwin & Bregman 2001, David et al. 2002). This trend may be somewhat stronger in cooling flow clusters (Irwin & Bregman 2001). Two of these studies were carried out using the low resolution ASCA and *BeppoSAX* observatories, and were based on radially-averaged trends between metallicity and radius. These trends suggest that the correlation between the presence of the cD and the central metallicity enhancement came about primarily as a result

of type one supernovae (SNe Ia) in the cD’s stellar populations, with some contribution of type two supernovae (SNe II) from star formation in the cooling flows.

In Figure 9, we show that there is a remarkable correlation between the location and shape of the Abell 1068 cD galaxy’s optical isophotes and the isometallicity contours. The strongly flattened appearance of both the isophotes and the metallicity contours renders a chance coincidence unlikely. It suggests strongly that the presence of the cD and regions of enhanced metallicity are strongly coupled. The average cluster metallicity beyond the cD is  $Z_0 \sim 0.4$ , in solar units, and rises to  $Z_{cD} \sim 0.8$  at the location of the cD. This metallicity increase has likely occurred either by the external introduction of enriched gas during a group merger or by an internal process related to mass loss from the stars in the cD or the cluster at large. Given the correlation between the cD’s optical isophotes and the contours of highest metallicity, we will examine whether mass loss from the general population of stars in the cD and the ongoing star formation would be capable of producing the observed metallicity enhancement.

We can characterize the metallicity of the keV gas in the vicinity of the cD as  $Z_{cD} = Z_0 + \delta Z$ , where  $\delta Z$  represents the metal enhancement due to supernova explosions, then

$$Z_{cD} \simeq Z_0 + \left( \frac{y_I + y_{II}}{M_H} \right) \times \left( \frac{M_Z}{M_H} \right)_{\odot}^{-1}. \quad (1)$$

In order to calculate the supernova type Ia rate, we adopt Tamman’s (1974) value  $4 \times 10^{-13} L_B \text{ yr}^{-1}$ . The integrated R-band absolute magnitude of the cD out to a 170 kpc radius is  $-24.0$ , which corresponds to  $L(R) = 2 \times 10^{11} L_{\odot}$ . Adopting an average color for a typical cD of  $(B-R) = 1.6$  (Peletier et al. 1990), we find an integrated B-band luminosity of  $L(B) = 1.4 \times 10^{11} L_{\odot}$ . This corresponds to a SNe Ia rate of  $0.03 \text{ yr}^{-1}$ . For the iron yield per SNe Ia we adopt  $0.74 M_{\odot}/\text{SNe I}$  (cf. David et al. 2001), giving a total yield of  $y_I \sim 2 \times 10^7 M_{\odot}(\text{t}/\text{Gyr})$ .

In addition to the yields from SNe Ia, there will be a significant contribution of metals from SNe II associated with the ongoing star formation in the cD. Assuming an iron yield of  $0.12 M_{\odot}/\text{SNeII}$ , and a supernova rate of 1 per  $100 M_{\odot}$  of star formation (cf. David et al. 2001), we obtain a total yield of  $y_{II} \sim 1.2 \times 10^{-3} M_{AP} M_{\odot}$ . Adopting the luminosity masses for the accretion populations in Table 2, we find  $y_{II} \sim 8 \times 10^5 - 4 \times 10^6 M_{\odot}$ . In order to match the observational constraints, the supernova yields must approximately double the ambient metallicity of  $\sim 0.4$  solar by seeding the ambient gas with metals. >From Figure 13, we find an integrated gas mass within a 170 kpc radius of  $3.4 \times 10^{12} M_{\odot}$ . Further adopting a solar iron abundance  $(M_Z/M_H)_{\odot} = 4.67 \times 10^{-5}$ , we find that the observed central abundance gradient would accrue after only  $\sim 3$  Gyr. This conclusion is largely independent of the SNe II yields from the starburst. Assuming SNe II yields from the maximum mass of the accretion population permitted by the data,  $M_{AP} = 3.1 \times 10^9 M_{\odot}$  (cf. Table 2), the mass ratio of SNe Ia to SNe II yields is 15. The implications of this result for the starburst in Abell 1068 is discussed in more detail in Paper II.

To summarize, the metallicity gradient associated with the cD galaxy can be almost entirely accounted for by type Ia supernovae originating in the ambient stellar population of the cD over a reasonable age for the galaxy. However, in the central starburst region, the SNe II yields from the starburst will become increasingly important. Furthermore, the central metallicity will almost certainly continue to grow as the roughly  $4 \times 10^{10} M_{\odot}$  of remaining molecular fuel (Edge 2001) is con-

sumed by star formation. We should emphasize the factors of several uncertainty in both the star formation masses, supernova rates, and yields. However, the numbers taken at face value, coupled with the observed correlation between the optical and metallicity isocontours, present persuasive case for cD galaxy-driven metallicity gradients in the keV gas.

#### 4. SURFACE BRIGHTNESS PROFILES

Despite the apparent spatial complexity evident in the core of Abell 1068, the overall surface brightness in the cluster can still be well described by an analytic  $\beta$  model profile. This profile combined with the temperature information from §3.2 can be used to determine the density profile, and various other physical properties of the ICM. Surface brightness profiles were calculated by constructing image mosaics of all chips in the observation in three bands: a total band image from 0.3-7.0 keV, and soft and hard bands spanning 0.3-2.0 keV and 2.0-7.0 keV, respectively. Point sources were filtered out as discussed in §2. Appropriately weighted exposure maps were then created for each band in order to accurately correct for variations in the detector efficiency over the field. Finally, the surface brightness profiles were calculated in elliptical annuli, 1 arcsec in width with a position angle and axis ratio as discussed in §2. The profiles were determined out to a maximum radius of 16.6 arcminutes or 2.8 Mpc.

Figure 10 shows the resulting surface brightness profile in the 0.3–7.0 keV band. Profiles for the soft and hard bands look similar. An inflection in the profile is apparent at a radius of  $\sim 10$  arcsec ( $\sim 25$  kpc). Attempts to fit the surface brightness profiles with single  $\beta$  models yielded unacceptable fits. Consequently, we have used a double  $\beta$  model of the form

$$I(r) = I_B + I_1 \left(1 + \frac{r^2}{r_1^2}\right)^{-3\beta_1 + \frac{1}{2}} + I_2 \left(1 + \frac{r^2}{r_2^2}\right)^{-3\beta_2 + \frac{1}{2}} \quad (2)$$

to describe the surface brightness profiles. Each component has fit parameters  $(I_i, r_i, \beta_i)$ , where the normalizations and core radii are denoted by  $I_i$  and  $r_i$ , respectively. The term  $I_B$  is a constant representing the contribution of the background. A detailed discussion of the double  $\beta$  model and its advantages for representing cluster X-ray surface brightness profiles can be found in Xue & Wu (2000) and Ettori (2000).

Table 2 shows the results from fitting equation 2 to the profiles for the total, soft, and hard bands. In all three bands, a broad component corresponding to the outer cluster gas is present with fit values of  $r_c \sim 24$  arcsecs for the core radius and  $\beta \sim 0.59$ , consistent within the measurement errors. For the total 0.3-7.0 keV, the fit to the inner component yielded values of  $r_c \sim 8$  arcsecs and  $\beta \sim 0.99$ . As Figure 11 illustrates, these two components are distinct at the 99% confidence level. Comparing the soft and hard band fits, we find that the inner  $\beta$  component in the soft, 0.3-2.0 keV band is more extended relative to the hard band with fit parameters of  $r_c \sim 11$  arcsec and  $\beta \sim 1.0$ . This extended soft core is consistent with the flattening of the temperature profile inside 10 arcsec discussed in §3.2 and shown in Figure 3. >From 2.0-7.0 keV, the best fit value of the core radius for the inner component is  $r_c \sim 4$  arcsecs, possibly due to the presence of non-thermal emission from the unresolved, central AGN or heating from the starburst. Reduced  $\chi^2$  values for the total, soft, and hard band fits were 1.8, 1.2, and 1.2, respectively.

We note that recent models of bubbles in cluster atmospheres associated with central AGN can produce “kinks” or inflections

in the azimuthally averaged surface brightness similar to that seen in Figure 10. However, no other obvious evidence for bubbles is apparent in the images of Abell 1068. Also, the strong correlation between the optical isophotes and the abundance map presented in Figure 9 is difficult to reconcile with significant mixing of the ICM due to bubbles.

#### 5. PHYSICAL CONDITIONS IN A1068

##### 5.1. Density Profile

Following the derivation of Xue & Wu (2000), we assume that the two  $\beta$  model components in equation 2 correspond to two phases of gas in the ICM with potentially different electron temperatures  $T_1$  and  $T_2$ . With this assumption, equation 2 can be inverted to yield the electron number densities for the two components as well as the combined electron number density,  $n_e(r)$ ,

$$n_e(r) = \sum_i n_{ei}(r) = \left[ n_e(0) \sum_i \tilde{n}_{ei}(r) \right]^{1/2}, \quad i = 1, 2 \quad (3)$$

$$n_{ei}(r) = \left[ \frac{n_e(0)}{n_e(r)} \right] \tilde{n}_{ei}(r) \quad (4)$$

$$\tilde{n}_{ei}(r) = n_{ei}(0) \left(1 + \frac{r^2}{r_i^2}\right)^{-3\beta_i} \quad (5)$$

where the core radii,  $r_i$ , and exponents,  $\beta_i$ , are the same as before and  $n_e(0)$  represents the central, total electron density. The central number densities for the individual components are related to the fitted surface brightness parameters,  $(I_i, r_i, \beta_i)$ , by

$$n_{ei}^2(0) = \left[ \frac{4\pi^{1/2}}{\alpha(T_i)g_i\mu_e} \right] \left[ \frac{\Gamma(3\beta_i)}{\Gamma(3\beta_i - 1/2)} \right] \left( \frac{I_i}{r_i} \right) A_{ij} \quad (6)$$

where

$$\frac{1}{A_{ij}} = 1 + \left( \frac{g_i}{g_j} \right) \left( \frac{r_i I_i}{r_j I_j} \right) \left( \frac{T_i}{T_j} \right)^{1/2} \left[ \frac{\Gamma(3\beta_i) \Gamma(3\beta_j - 1/2)}{\Gamma(3\beta_j) \Gamma(3\beta_i - 1/2)} \right], \quad (7)$$

$j = 1, 2 \text{ and } j \neq i$

and  $g_i$  is the Gaunt factor for component  $i$  and  $\alpha(T)$  is the emissivity due to thermal bremsstrahlung as given in Xue & Wu (2000).

The choice of values for  $T_1$  and  $T_2$  is somewhat uncertain; however, as equations 6 and 7 indicate, the temperature dependence of the central electron densities is fairly weak. We have chosen the minimum and maximum temperature values from the deprojected temperature profile discussed in §3.3 for the narrow and extended components, respectively. Using  $T_1 = 1.76$  keV and  $T_2 = 5.0$  keV, we obtain central densities of  $n_{e1}(0) = 0.135 \text{ cm}^{-3}$  and  $n_{e2}(0) = 0.024 \text{ cm}^{-3}$ . The resulting density profiles are shown in Figure 12. We note that using the two temperatures derived from the two-phase model (2T) fits in Table 1 resulted in central densities within 5% of these values. Of course, if the gas is truly multiphase as the spectral analysis in §3.1 indicates, then representing the temperature structure using only two components is simplistic. However, the observed surface brightness profile does not allow additional components to be unambiguously identified.

Using the derived density profiles, the spectral fitting results of Table 1, and the assumption of hydrostatic equilibrium, we have computed various estimates for the gas and total mass in Abell 1068. Table 3 gives the gas mass and total mass within 0.5 Mpc for the various spectral models discussed in §3.1 following the method discussed in Hicks et al. (2002). Figure 13

shows the gas mass profile for the best fit FC model. In addition to the total cluster estimates, we have calculated the mass associated with the central, condensed  $\beta$  model component separately. These estimates are labeled “Core” in Table 3 and assume a central temperature of 1.76 keV taken from the deprojected temperature profile discussed in §3.3.

### 5.2. Cooling Time

The characteristic time that it takes a plasma to cool isobarically through an increment of temperature  $\delta T$  can be written

$$t_{cool} = \frac{5}{2} \frac{k \delta T}{n_e \Lambda(T)} \quad (8)$$

where  $n_e$  is the electron density,  $\Lambda(T)$  is the total emissivity of the plasma (the cooling function), and  $k$  is Boltzmann’s constant. For isochoric cooling, 5/2 is replaced by 3/2. Utilizing the temperature profile from §3.2 and the density profile from §5.1, we can calculate the cooling time as a function of radius in the cluster. Figure 12 shows the resulting cooling time as a function of radius in Abell 1068. The central cooling time in the core reaches a minimum value of  $9 \times 10^7$  yrs. The “cooling radius” where the cooling time exceeds the age of the cluster, canonically taken to be  $10^{10}$  yrs, is 282 kpc. As we show in Paper II, 98% of the blue light associated with star formation in Abell 1068 occurs inside the central  $\sim 40$  kpc where the cooling time is  $\leq 5 \times 10^8$  yrs.

### 5.3. Entropy

Similarly, we can use the density and temperature information to calculate the entropy in the cluster gas as a function of position using

$$S = T/n^{2/3} \quad (9)$$

where  $T$  is given in keV. Figure 12 shows the resulting entropy profile. This figure shows what is becoming an ubiquitous feature of cluster cores, an “entropy floor” in the central regions. Inside of  $\sim 20$  kpc, the gas is essentially isentropic. Various mechanisms have been proposed to explain the presence of this entropy floor including pre-heating of the gas (Kaiser 1991) by supernovae-driven winds (e.g. Ponman, Cannon, & Navarro 1999) and active galactic nuclei (e.g. Yamada & Fujita 2001; Nath & Roychowdhury 2002). Alternatively, it has been argued that radiative cooling can be an efficient means for introducing an entropy floor at the observed levels. Voit et al. (2002) have studied the effect various entropy modifications on the properties of the cluster gas.

## 6. CONDUCTION

XMM RGS and *Chandra* HETG observations of cluster cores have failed to detect emission lines from gas at temperatures less than about 3 keV indicating that cooling may be truncated somehow (Peterson et al. 2001, Peterson et al. 2003, Wise et al. 2004). These data have led to the revitalization of various heating mechanisms previously considered to be ineffective in clusters including heating by the central AGN and thermal conduction. Recent work by Narayan & Medvedev (2001) and Zakamska & Narayan (2003) however suggests that thermal conduction may be effective in clusters. Using the derived density and temperature in the cluster, we can directly calculate the heat input due to thermal conduction in Abell 1068. Following the analysis of Zakamska & Narayan (2003), we can write

$$F = -\kappa \frac{dT}{dr} \quad (10)$$

for the heat flux due to thermal conduction, where the thermal conductivity is

$$\kappa = f \kappa_{sp} = f \left( \frac{1.84 \times 10^{-5} T^{5/2}}{\ln \Lambda} \right) \text{ ergs s}^{-1} \text{ K}^{-1} \text{ cm}^{-1} \quad (11)$$

and  $\ln \Lambda \sim 37$  is the usual Coulomb logarithm. Here, the conductivity is expressed relative to the canonical Spitzer value,  $\kappa_{sp}$  by a fixed fraction  $f$ . Figure 14 shows the resulting conductive heat flux as a function of radius in the cluster assuming  $f = 1$ , i.e. assuming thermal conduction is operating at the Spitzer value. The heat flux peaks at a radius of  $\sim 50$  kpc where the temperature gradient is steepest.

A more interesting quantity to calculate, however, is the required level of thermal conduction necessary to balance cooling. If we assume that the observed X-ray luminosity due to cooling within a given radius is completely balanced by heating due to thermal conduction from hotter gas outside that radius, we can write

$$L_X(< r) = 4\pi r^2 f \kappa_{sp} \left( \frac{dT}{dr} \right). \quad (12)$$

Solving this equation for the required value of the conduction parameter,  $f$ , at each position in the cluster yields Figure 15. As this figure shows, the thermal conductivity of the gas must exceed the Spitzer value by an order of magnitude to balance radiative cooling over the cooling radius in Abell 1068. Consequently, it seems unlikely that thermal conduction could quench cooling in Abell 1068, especially in the core. Similar results have been found for analyses of other cooling flow clusters observed by *Chandra* including Abell 2052, Abell 2597, Hydra A, Ser 159-03, and 3C 295 (Zakamska & Narayan 2003) as well as the cores of Abell 2199 and Abell 1835 (Voigt et al. 2002; Fabian, Voigt, & Morris 2002). As we show in Paper II, energy input from other sources such as the central AGN and supernovae can account for  $\leq 25\%$  of the X-ray luminosity from cooling gas.

## 7. CONCLUSIONS

We have performed a detailed spatial and spectral analysis of a 26.8 ksec *Chandra* X-ray observation of the Abell 1068 cluster of galaxies. This cluster is exceptional due to the presence of a massive 20–70  $M_\odot \text{ yr}^{-1}$  starburst in the core. Our primary goal was to determine whether or not the data for this object are consistent with the standard cooling flow model where cooling X-ray plasma accumulates in some cold form such as stars. Our analysis indicates that Abell 1068 exhibits many of the common characteristics seen in other clusters with cool cores including a sharply peaked surface brightness profile, declining temperature gradient, and flat entropy profile in the core. Although discriminating between various spectral models can be difficult at CCD resolutions, the integrated X-ray spectrum for Abell 1068 is best fit by a cooling flow model with a total mass deposition rate of  $\sim 150 M_\odot \text{ yr}^{-1}$ . Inside a radius of 40 kpc, the measured cooling rate drops to  $\sim 40 M_\odot \text{ yr}^{-1}$  which is completely consistent with the star formation rates.

Although measuring mass deposition rates from X-ray data is notoriously difficult to interpret due to the degeneracy in spectral fits, the cooling time in the gas is a well constrained quantity. The X-ray surface brightness distribution for Abell 1068 provides an accurate measure of the density in the gas. When combined with the measured temperature profile, we find

that the cooling time of the gas in the core of Abell 1068 is very short, reaching a minimum of  $9 \times 10^7$  yrs. The cooling time inside 40 kpc, where 98% of the star formation is observed in Abell 1068 occurs (Paper II), is  $\leq 5 \times 10^8$  yrs. The close spatial correspondence between regions of observed star formation and short cooling times again points to a connection between the cooling X-ray plasma and the star forming material.

The abundance profile in Abell 1068 is especially striking. The annular analysis clearly indicates a central enhancement in the core roughly a factor of 2 higher than in the outer regions. We have also constructed a 2D map of the abundance in the cluster which shows a strong spatial correlation with the optical light. Our analysis indicates that this central increase is consistent with enhancement by supernova explosions associated with the cD's ambient stellar population and the recent starburst. This correlation also argues against the presence of significant energy input due to "bubbles" generated by a central AGN, since such a mechanism would tend to smooth out such enhancements on a relatively short timescale. And in any event, the central radio source in Abell 1068 is an order of magnitude weaker than those in clusters like Hydra A and Perseus where such bubbles are observed.

Finally, we have examined the possibility that heating by thermal conduction could quench cooling in this object. We find that conduction is an order of magnitude too weak to balance the emission from cooling over the entire cooling region. In Paper II, we have examined various other potential feedback mechanisms including the central AGN and energy input from supernovae. We estimate that these mechanisms could account for  $\lesssim 25\%$  of the cooling luminosity. Taken all together, these results are consistent with a picture where the extreme starburst properties of Abell 1068 are being fueled by a cooling ICM.

The authors would like to thank John Houck for many helpful discussions and a variety of technical support. M. Wise was supported by the Smithsonian Astrophysical Observatory (SAO) contract SVI-61010 for the Chandra X-Ray Center (CXC). B. McNamara was supported by NASA Long Term Space Astrophysics Grant NAG5-11025 and Chandra Archival Research Grant AR2-3007X. S. Murray was supported by NASA Grant NAS8-01130.

#### REFERENCES

- Allen, S. W., Etori, S., Fabian, A. C. 2001, MNRAS, 324, 877.  
 Arnaud, K.A., 1996, Astronomical Data Analysis Software and Systems V, eds. Jacoby G. and Barnes J., p17, ASP Conf. Series volume 101.  
 Brighenti, F. & Mathews, W. G. 2002, ApJ, 574, L11.  
 Cardiel, N., Gorgas, J., & Aragon-Salamanca, A. 1998, MNRAS, 298, 977.  
 Crawford, C. S., Allen, S. W., Ebeling, H., Edge, A. C., Fabian, A. C. 1999, MNRAS, 306, 857.  
 David, L. P., Nulsen, P. E. J., McNamara, B. R., Forman, W., Jones, C., Ponman, T., Robertson, B., Wise, M. 2001, ApJ, 557, 546.  
 Donahue, M., Mack, J., Voit, G. M., Sparks, W. B., Elston, R., & Maloney, P. R. 2000, ApJ, 545, 670.  
 Edge, A. C. 2001, MNRAS, 328, 762.  
 Etori, S. 2000 MNRAS, 318, 1041.  
 Fabian, A. C. 1994, ARAA, 32, 277.  
 Fabian, A. C., Mushotzky, R. F., Nulsen, P. E. J., Peterson, J. R. 2000, MNRAS, 321, L20.  
 Fabian, A. C., Voit, L. M., Morris, R. G. 2002, MNRAS, 335, 71.  
 Falcke, H., Rieke, M. J., Rieke, G. H., Simpson, C., Wilson, A. 1998, ApJ, 494, 155.  
 Fukazawa, Y., Makishima, K., Tamura, T., Nakazawa, K., Ezawa, H., Ikebe, Y., Kikuchi, K., & Ohashi, T. 2000, MNRAS, 313, 21.  
 Hicks, A. K., Wise, M. W., Houck, J. C., Canizares, C. R. 2002, ApJ, 580, 763.  
 Houck, J. C. & Denicola, L. A. 2000, ASP Conf. Ser. 216: Astronomical Data Analysis Software and Systems IX, 9, 591.  
 Houck, J.C., Davis, D. S., Wise, M. W. 2004, ApJ, in preparation.  
 Irwin, J. A., & Bregman, J. N., 2001, ApJ, 546, 150.  
 Jaffe, W. & Bremer, M. N. 1997, MNRAS, 284, L1.  
 Jaffe, W. & Bremer, M. N., & van der Werf, P. P. 2001, MNRAS, 324, 443.  
 Johnstone, R. M., Allen, S. W., Fabian, A. C., Sanders, J. S. 2002, in press (astro-ph/0202071).  
 Kaiser, N. 1991, ApJ, 383, 104.  
 Markevitch, M., Ponman, T. J., Nulsen, P. E. J., Bautz, M. W., Burke, D. J., David, L. P., Davis, D., Donnelly, R. H., Forman, W. R., Jones, C., Kaastra, J., Kellogg, E., Kim, D.-W., Kolodziejczak, J., Mazzotta, P., Pagliaro, A., Patel, S., Van Speybroeck, L., Vikhlinin, A., Vrilek, J., Wise, M., & Zhao, P. 2000, ApJ, 541, 542.  
 McNamara, B. R. 2002, in "The High Energy Universe at Sharp The High Energy Universe at Sharp Focus: Chandra Science," San Francisco: ASP Conf. Ser., 262, 351, eds. S. Vrilek, E. M. Schlegel, & L. Kuhi, astro-ph/0202199.  
 McNamara, B. R. & O'Connell, R. W. 1989, AJ, 98, 2018.  
 McNamara, B. R., Wise, M., Nulsen, P. E. J., David, L. P., Sarazin, C. L., Bautz, M., Markevitch, M., Vikhlinin, A., Forman, W. R., Jones, C., & Harris, D. E. 2000, ApJ, 534, L135.  
 McNamara, B. R., Wise, M. W., Murray, S. S. 2004, ApJ, in press.  
 Nath, B. B. & Roychowdhury, S. 2002, MNRAS, 333, 145.  
 Narayan, R. & Medvedev, M. V. 2001, ApJ, 562, 129.  
 Nulsen, P. E. J., David, L. P., McNamara, B. R., Jones, C., Forman, W.R., & Wise, M. 2002, ApJ, 568, 163.  
 Peletier, R. F., Davies, R. L., Illingworth, G. D., Davis, L. E., & Cawson, M. 1990, AJ, 100, 1091.  
 Peterson, J. R., Paerels, F. B. S., Kaastra, J. S., Arnaud, M., Reiprich, T. H., Fabian, A. C., Mushotzky, R. F., Jernigan, J. G., Sakelliou, I. 2001, A&A, 365, 104.  
 Peterson, J. R., Kahn, S. M., Paerels, F. B. S., Kaastra, J. S., Tamura, J. A. M., Bleeker, & C. Ferrigno 2003, ApJ, submitted, astro-ph/0210662.  
 Ponman, T. J., Cannon, D. B., & Navarro, J. F. 1999, Nature, 397, 135.  
 Ruszkowski, M. & Begelman, M. C. 2002, ApJ, 581, 223.  
 Smith, R. K., Brickhouse, N. S., Liedahl, D. A., Raymond, J. C. 2001, ApJ, 556, L91.  
 Tammann, G. A. 1974, in Supernovae and Supernova Remnants, Proceedings of the International Conference on Supernovae, Dordrecht: Reidel, ed. by C. B. Cosmovici, Astrophysics and Space Science Library, Vol. 45, 155.  
 Vikhlinin, M., Markevitch, M., Murray, S. S. 2001, ApJ, 551, 160.  
 Voit, L. M., Schmidt, R. W., Fabian, A. C., Allen, S. W., Johnstone, R. M., MNRAS, 335, 7.  
 Voit, G. M., Bryan, G. L., Balogh, M. L., & Bower, R. G. 2002, ApJ, 576, 601.  
 Wise, M. W., Houck, J. C., Canizares, C. R., Hicks, A. K. 2004, in preparation.  
 Wise, M. W., Houck, J. C. 2004, in preparation.  
 Xue, Y.-J., Wu, X.-P., 2000 MNRAS, 318, 715.  
 Yamada, M. & Fujita, Y. 2001, ApJ, 553, 145.  
 Zakamska, N. L., & Narayan, R. 2003, ApJ, 582, 162.



TABLE 1  
INTEGRATED SPECTRAL FITS

Model	$N_H^a$	$kT^b$	$A$	$kT_{min}^b$	$\dot{M}_X$	$\chi^2_{norm}$
1T	$1.26^{+0.45}_{-0.54}$	$3.76^{+0.22}_{-0.14}$	$0.47^{+0.08}_{-0.05}$	—	—	1.26
1T	1.40	$3.76^{+0.13}_{-0.14}$	$0.47^{+0.05}_{-0.05}$	—	—	1.25
2T	$1.39^{+0.33}_{-0.58}$	$6.85^{+2.15}_{-1.92}$	$0.38^{+0.07}_{-0.06}$	$2.16^{+0.46}_{-0.44}$	—	1.15
2T	1.40	$6.84^{+2.16}_{-1.86}$	$0.38^{+0.06}_{-0.06}$	$2.16^{+0.45}_{-0.43}$	—	1.13
FC	$2.21^{+0.53}_{-0.52}$	$4.21^{+0.21}_{-0.20}$	$0.50^{+0.06}_{-0.06}$	0.10	$145.09^{+41.87}_{-36.77}$	1.12
FC	1.40	$4.27^{+0.18}_{-0.22}$	$0.54^{+0.05}_{-0.07}$	0.10	$114.07^{+26.05}_{-33.42}$	1.14
TC	$1.19^{+0.59}_{-0.27}$	$5.92^{+0.66}_{-1.01}$	$0.44^{+0.06}_{-0.07}$	2.00	$983.39^{+131.93}_{-103.57}$	1.19
TC	1.40	$5.96^{+0.00}_{-0.81}$	$0.43^{+0.05}_{-0.05}$	2.00	$1038.06^{+73.97}_{-17.55}$	1.16
VC	$1.27^{+0.39}_{-0.41}$	$7.51^{+0.03}_{-1.67}$	$0.40^{+0.06}_{-0.04}$	$1.45^{+0.38}_{-0.00}$	$790.44^{+13.26}_{-9.20}$	1.14
VC	1.40	$7.54^{+0.00}_{-1.59}$	$0.40^{+0.04}_{-0.04}$	$1.48^{+0.35}_{-0.01}$	$805.63^{+27.32}_{-0.00}$	1.13

<sup>a</sup>Galactic column in units of  $10^{20} \text{ cm}^{-2}$ .

<sup>b</sup>Temperature in keV.

TABLE 2  
BETA-MODEL FITS

$\Delta E$ [keV]	$r_1$ ["]	$\beta_1$	$I_1^a$	$r_2$ ["]	$\beta_2$	$I_2^a$	$I_B^a$	$\chi_{\text{norm}}^2$	$\chi^2$	N
0.29–7.00	$24.19^{+1.91}_{-1.55}$	$0.598^{+0.006}_{-0.006}$	$1294.9^{+156.72}_{-186.08}$	$7.65^{+1.53}_{-1.28}$	$0.990^{+0.198}_{-0.165}$	$7717.4^{+527.77}_{-482.84}$	$2.542^{+0.04}_{-0.04}$	1.77	723.7	417
0.29–2.00	$21.27^{+1.40}_{-1.09}$	$0.587^{+0.006}_{-0.005}$	$1239.5^{+103.43}_{-124.34}$	$10.96^{+2.19}_{-1.83}$	$1.665^{+0.333}_{-0.278}$	$5950.4^{+404.37}_{-364.17}$	$1.050^{+0.03}_{-0.03}$	1.19	486.0	416
2.00–7.00	$26.37^{+5.11}_{-3.06}$	$0.574^{+0.035}_{-0.015}$	$193.0^{+38.61}_{-32.17}$	$4.38^{+0.88}_{-0.73}$	$0.554^{+0.111}_{-0.055}$	$1377.6^{+267.37}_{-219.51}$	$1.458^{+0.03}_{-0.03}$	1.19	488.6	417

<sup>a</sup>Surface brightness  $I$  in units of  $10^{-9}$  photons  $\text{sec}^{-1} \text{cm}^{-2} \text{arcsec}^{-2}$

TABLE 3  
MASS ESTIMATES

Model	$kT$ [keV]	$n_0$ [ $10^{-2} \text{ cm}^{-3}$ ]	$M_{gas}$ [ $10^{13} M_{\odot}$ ]	$M_{tot}$ [ $10^{13} M_{\odot}$ ]
1T	$3.76^{+0.22}_{-0.14}$	$2.40^{+0.17}_{-0.17}$	$4.72^{+0.90}_{-0.80}$	$25.28^{+1.99}_{-1.95}$
2T	$6.85^{+2.15}_{-1.92}$	$2.38^{+0.17}_{-0.17}$	$4.68^{+0.89}_{-0.79}$	$45.45^{+12.08}_{-11.66}$
FC	$4.21^{+0.21}_{-0.20}$	$2.44^{+0.17}_{-0.18}$	$4.81^{+0.91}_{-0.82}$	$27.41^{+2.31}_{-2.24}$
TC	$5.92^{+0.66}_{-1.01}$	$2.37^{+0.17}_{-0.17}$	$4.67^{+0.89}_{-0.79}$	$41.21^{+7.63}_{-7.27}$
Core	$1.76^{+0.21}_{-0.10}$	$13.53^{+1.56}_{-1.38}$	$0.15^{+0.32}_{-0.10}$	$19.77^{+5.64}_{-4.68}$

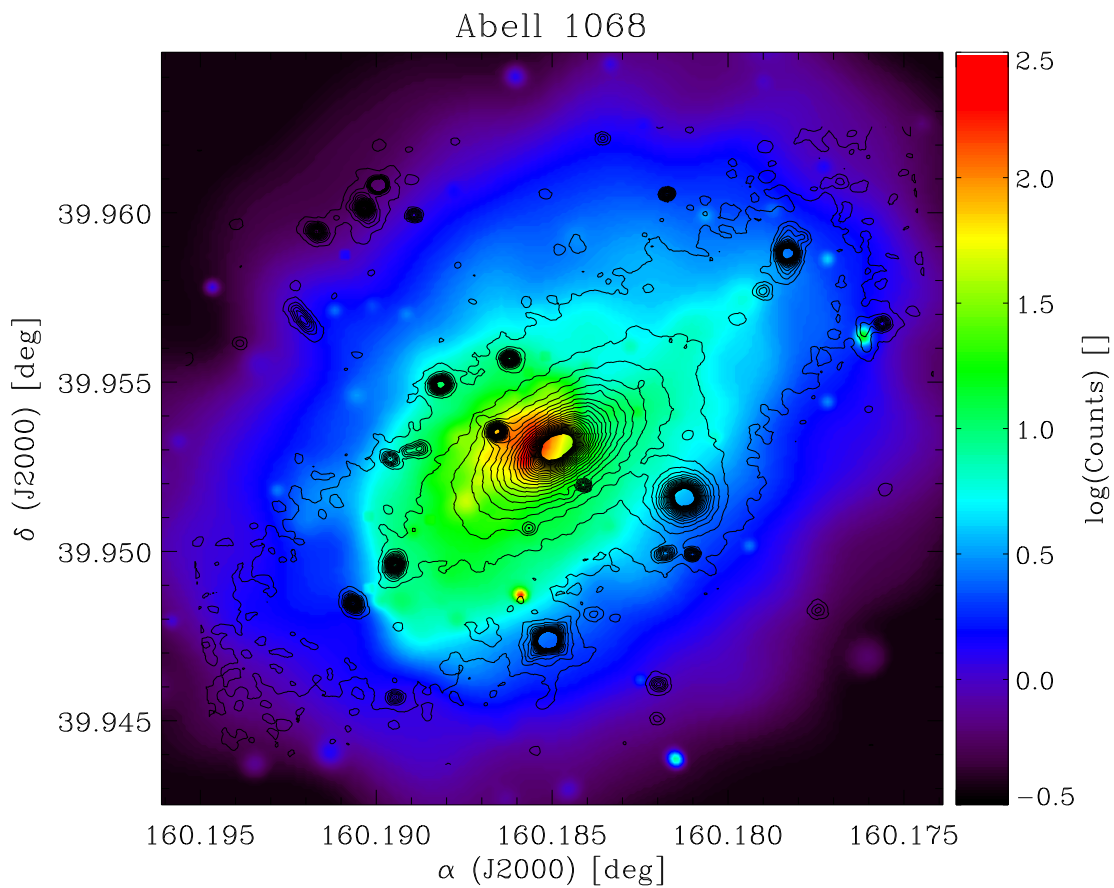


FIG. 1.— An exposure corrected, 0.3-7.0 keV image of the central  $80'' \times 80''$  of Abell 1068 from the 26.8 ksec ACIS-S exposure. The image has been adaptively smoothed using the CIAO tool `CSMOOTH`. The optical contours corresponding to the HST R-band (F606W) surface brightness are also shown. Note the offset between the X-ray centroid and the optical center of the cD galaxy.

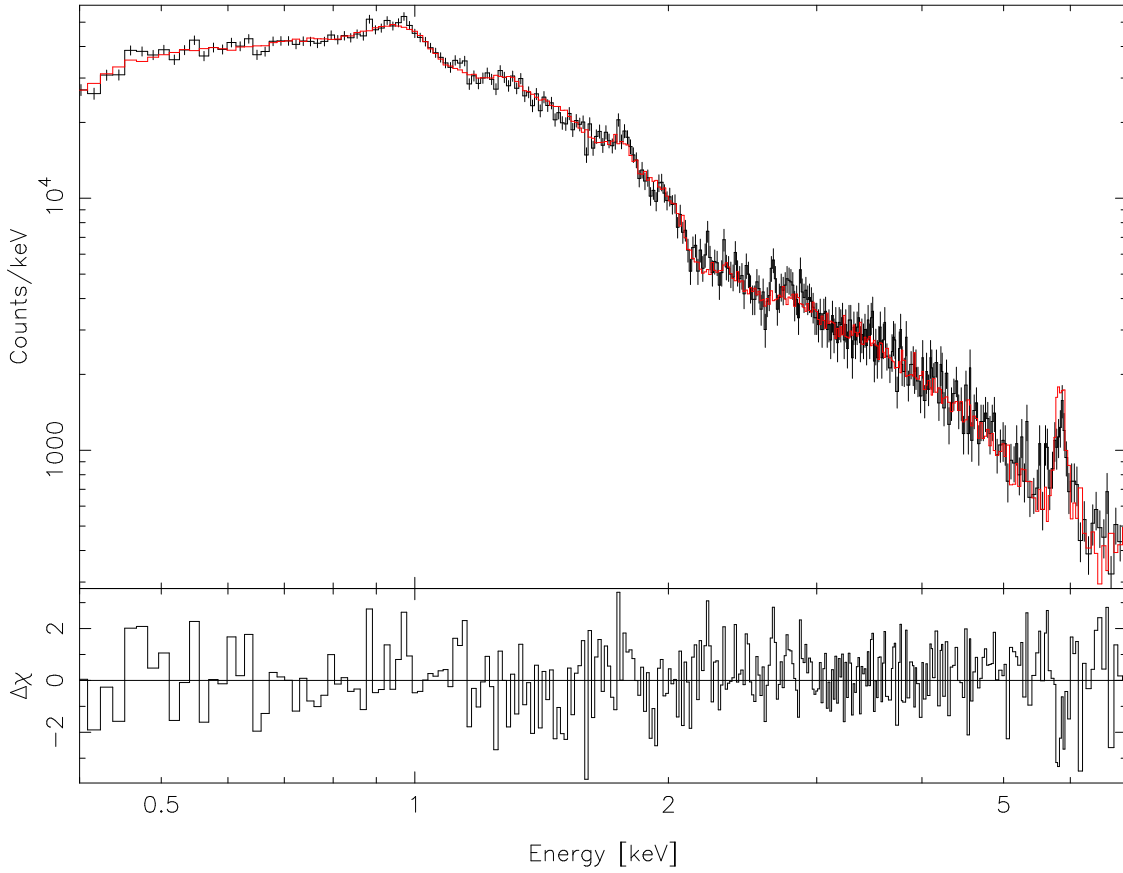


FIG. 2.— Integrated 0.3–7.0 keV spectrum for Abell 1068 from the  $175 \times 129$  arcsec elliptical extraction region discussed in the text. The spectrum has been adaptively binned to contain 30 counts per bin. The solid line shows the best fit spectral model, in this case the FC cooling flow model discussed in the text.

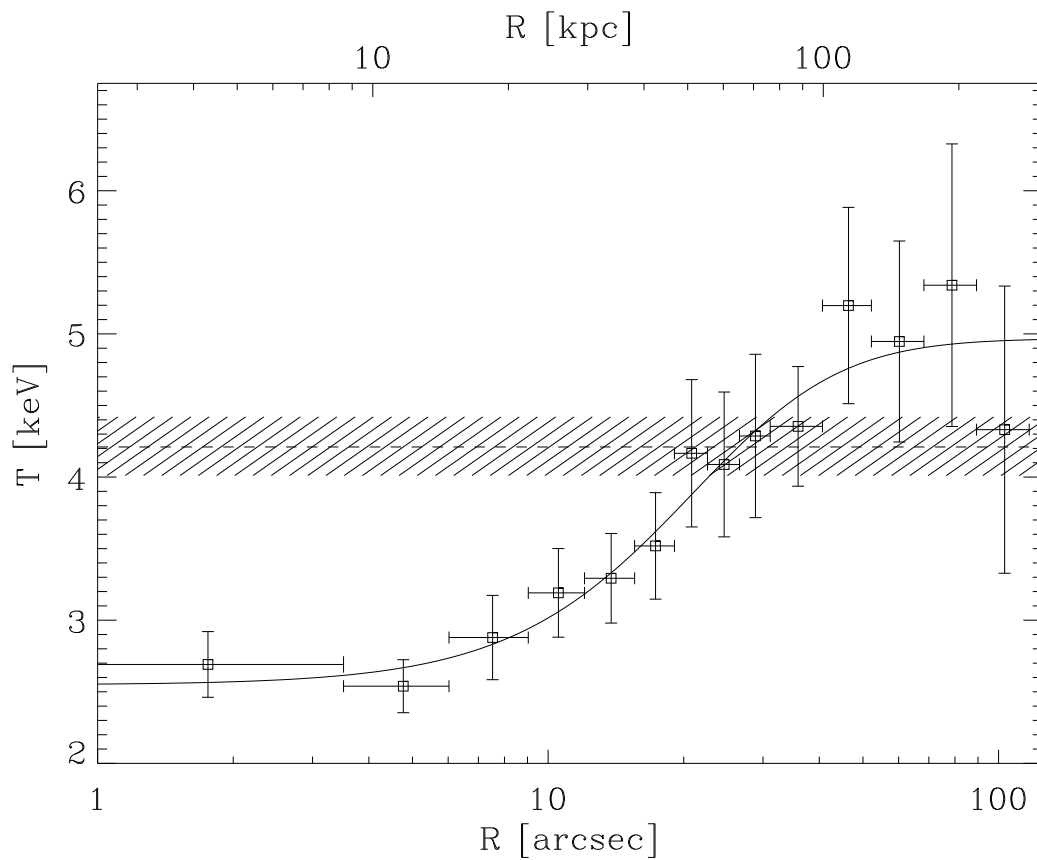


FIG. 3.— The projected gas temperature for Abell 1068 as a function of projected radius along the semi-major axis in the cluster. One sigma errors bars are indicated. The horizontal dashed line marks the mean gas temperature from the best fit to the integrated spectrum shown in Figure 2, while the hatched horizontal region depicts the 90% confidence interval for the temperature. The solid line shows the best fit analytic model.

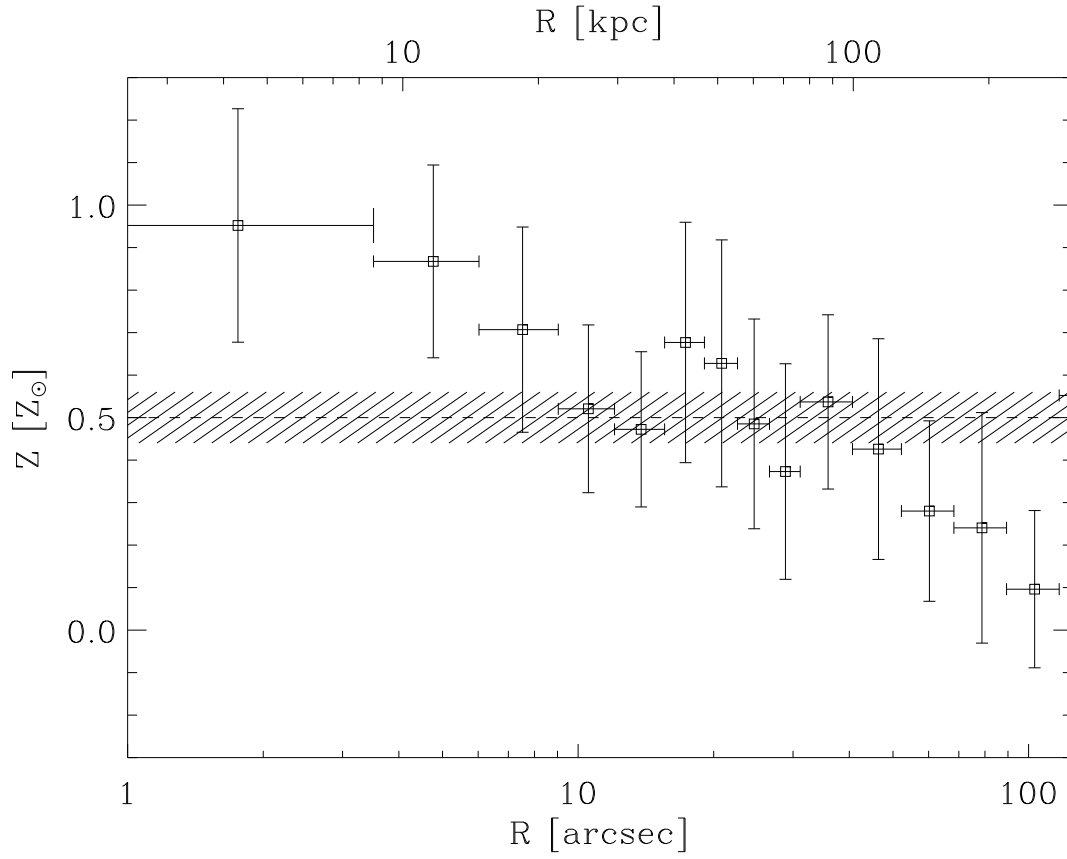


FIG. 4.— The projected abundance profile for Abell 1068 as a function of projected radius along the semi-major axis in the cluster. One sigma errors bars are indicated. The horizontal dashed line marks the mean abundance from the best fit to the integrated spectrum, while the hatched horizontal region depicts the 90% confidence interval for the mean abundance.

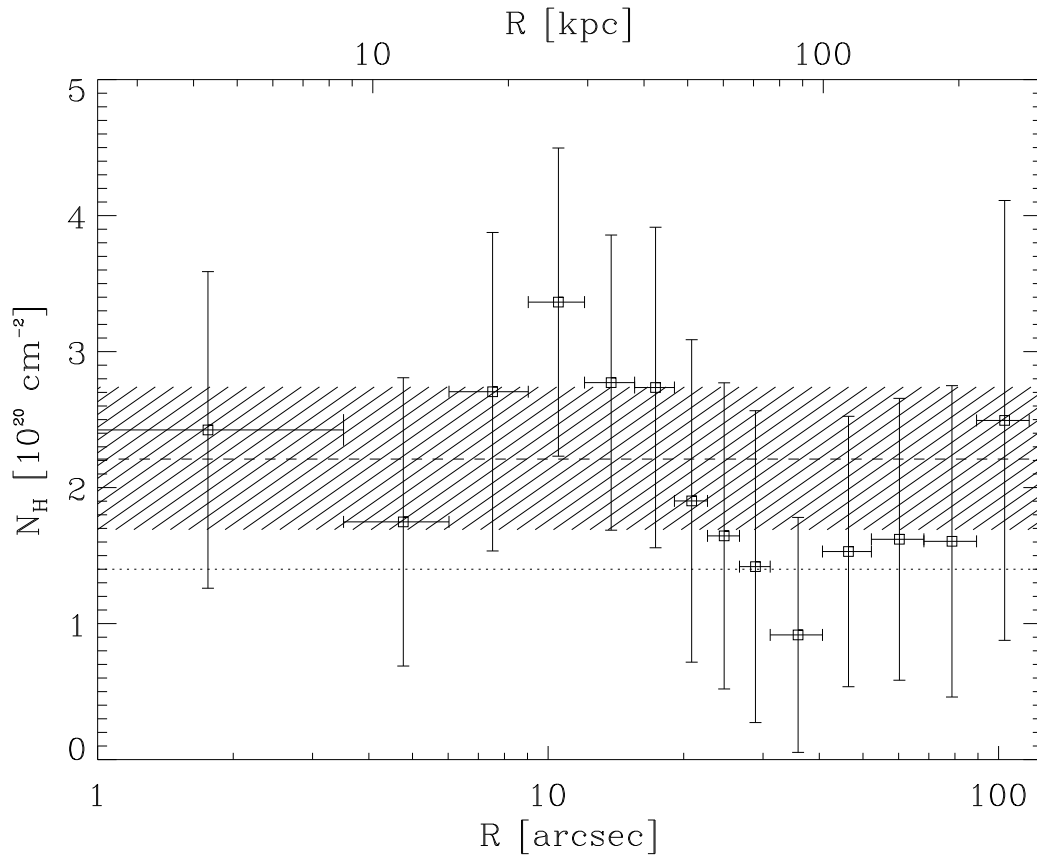


FIG. 5.— The best fit foreground absorbing column in Abell 1068 as a function of projected radius along the semi-major axis in the cluster. One sigma errors bars are indicated. The horizontal dashed line marks the column from the best fit to the integrated spectrum, while the hatched horizontal region depicts the 90% confidence interval for the mean column.



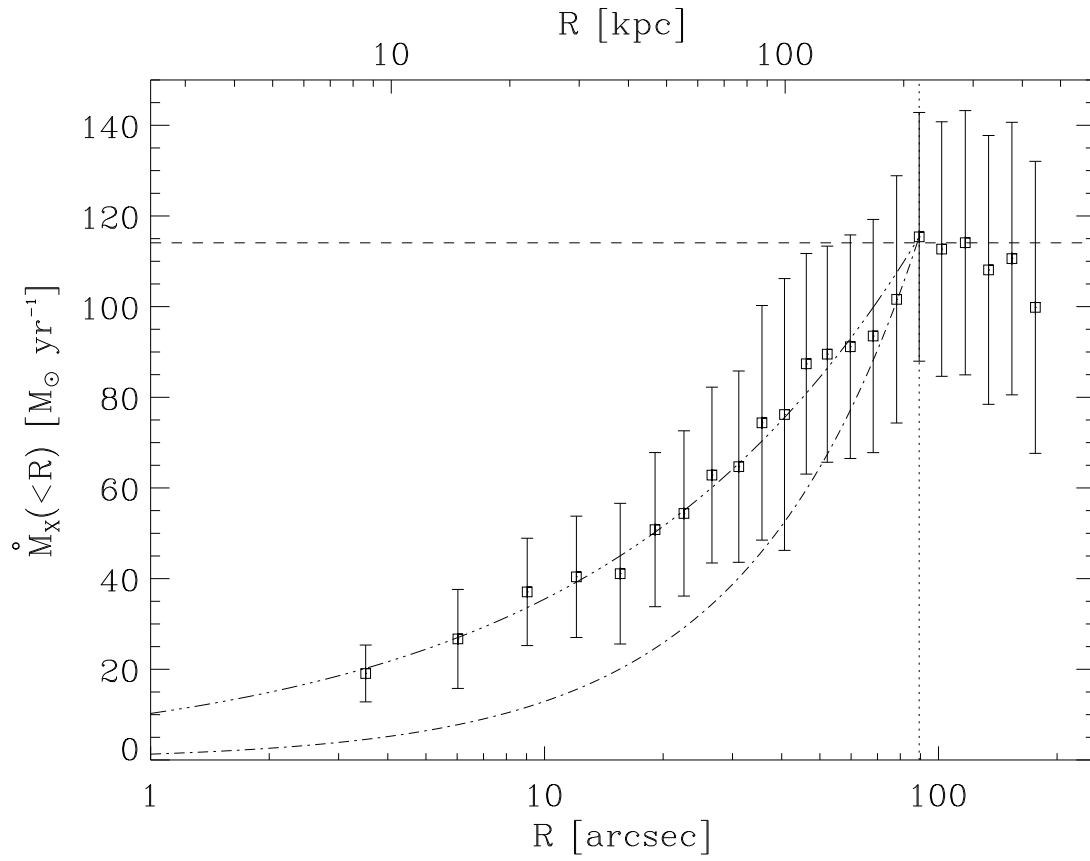


FIG. 6.— The enclosed mass deposition rate for Abell 1068 as a function of projected radius along the semi-major axis in the cluster. One sigma errors bars are indicated. The horizontal dashed line indicates the total deposition rate from the best-fit FC cooling flow model discussed in the text. The vertical dotted line marks the cooling radius as derived from the temperature and density profiles. Two analytic forms for  $\dot{M}_X(<r)$  are depicted by the dot-dashed and dot-dot-dot-dashed lines: the canonical  $\dot{M}_X(<r) \propto r$ , which does not describe the profile well, and  $\dot{M}_X(<r) \propto r^{0.4}$ , respectively.

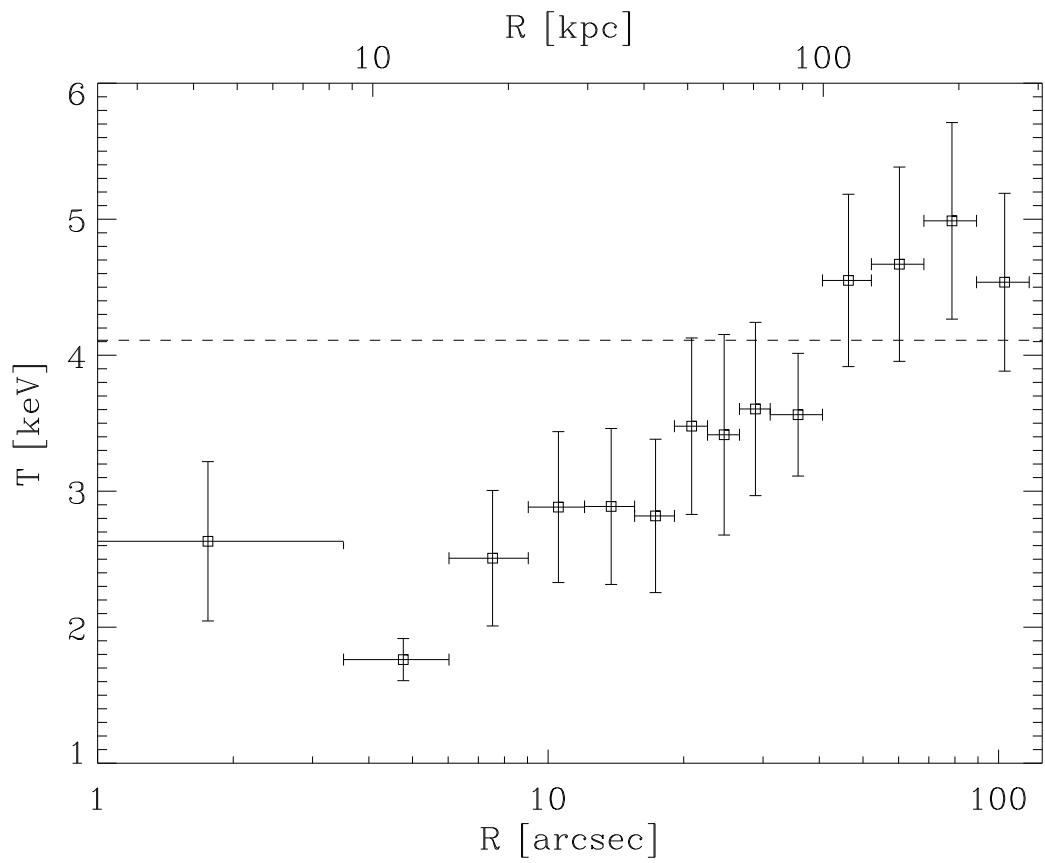


FIG. 7.— The deprojected gas temperature for Abell 1068 as a function of projected radius along the semi-major axis in the cluster. One sigma errors bars are indicated. The horizontal dashed line marks the mean gas temperature from the best fit to the integrated spectrum shown in Figure 2.

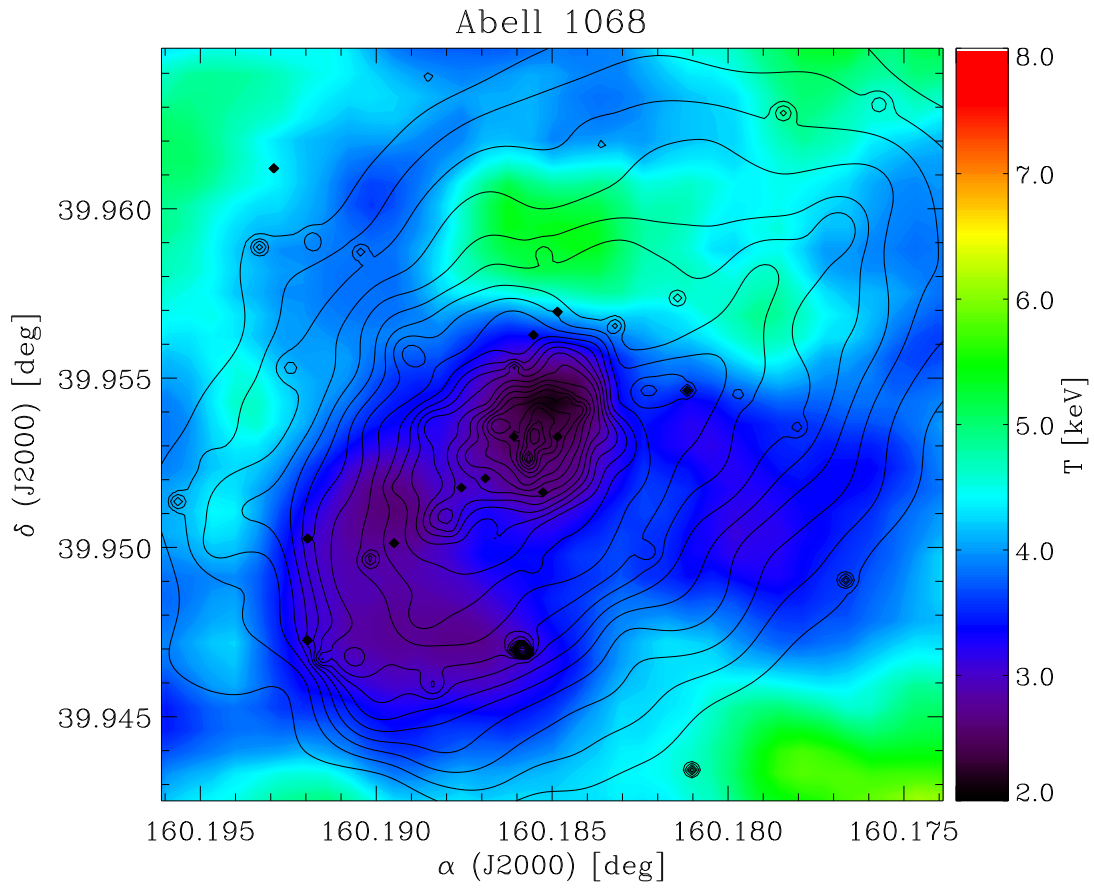


FIG. 8.— A map of the gas temperature for the central  $80'' \times 80''$  in Abell 1068. The overlaid contours show the surface brightness from the adaptively smoothed flux image shown in Figure 1. The color bar on the right indicates the temperature scale in keV. Errors for the measured temperatures range from 10%—30% over the map.

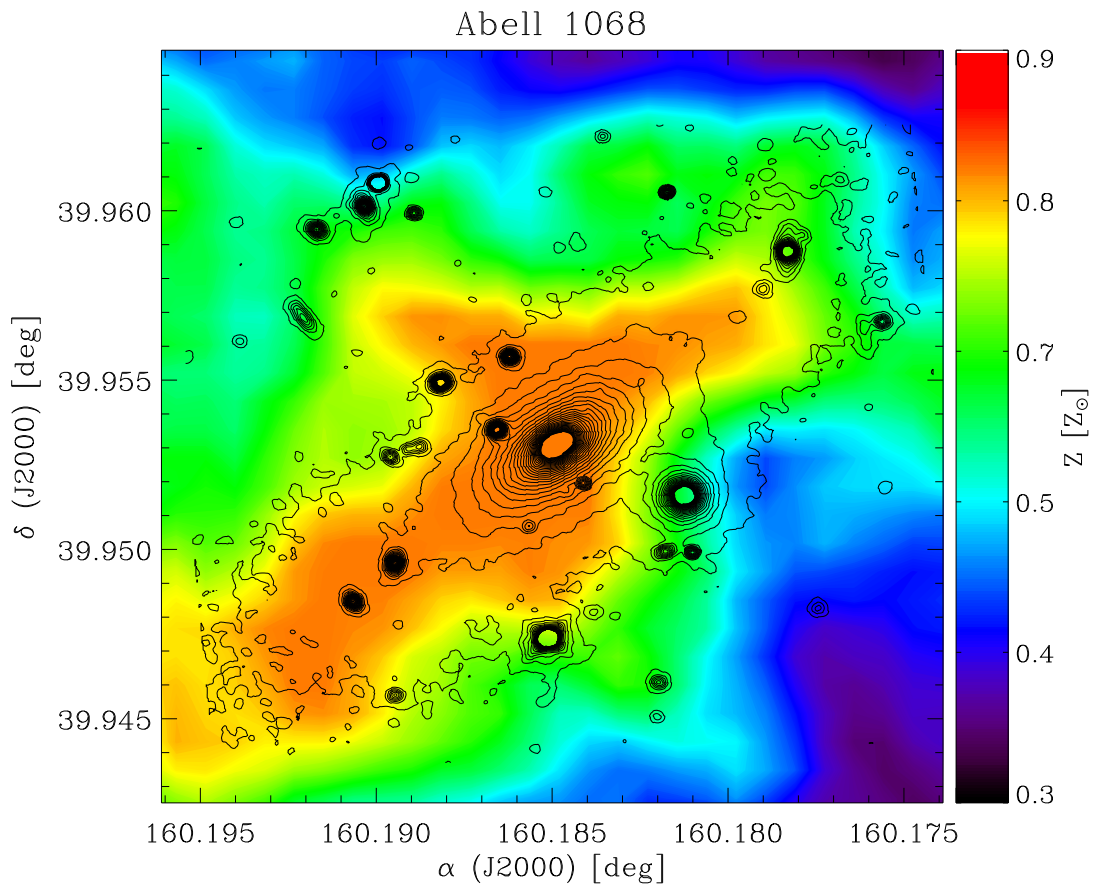


FIG. 9.— A map of the elemental abundance for the central  $80'' \times 80''$  in Abell 1068. The optical contours corresponding to the HST R-band (F606W) surface brightness are shown. The color bar on the right indicates the abundance in units of solar abundance. Errors for the measured abundances range from 10%—30% over the map.

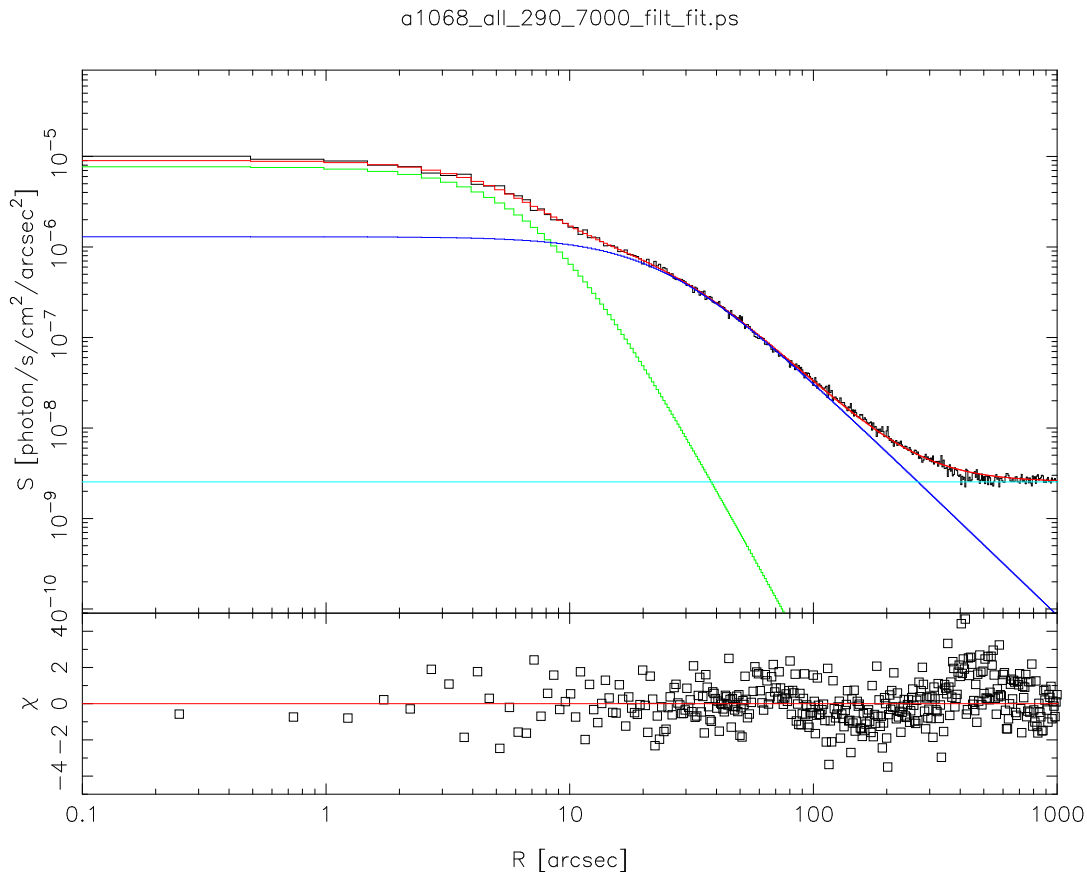


FIG. 10.— Radial surface brightness for Abell 1068 in the 0.3-7.0 keV band accumulated in 1 arcsec annular bins. The solid lines indicate the two components of the best fit double  $\beta$  model discussed in the text. The horizontal dotted line represents the best fitting background value. The lower pane shows the residual deviations from the fit.

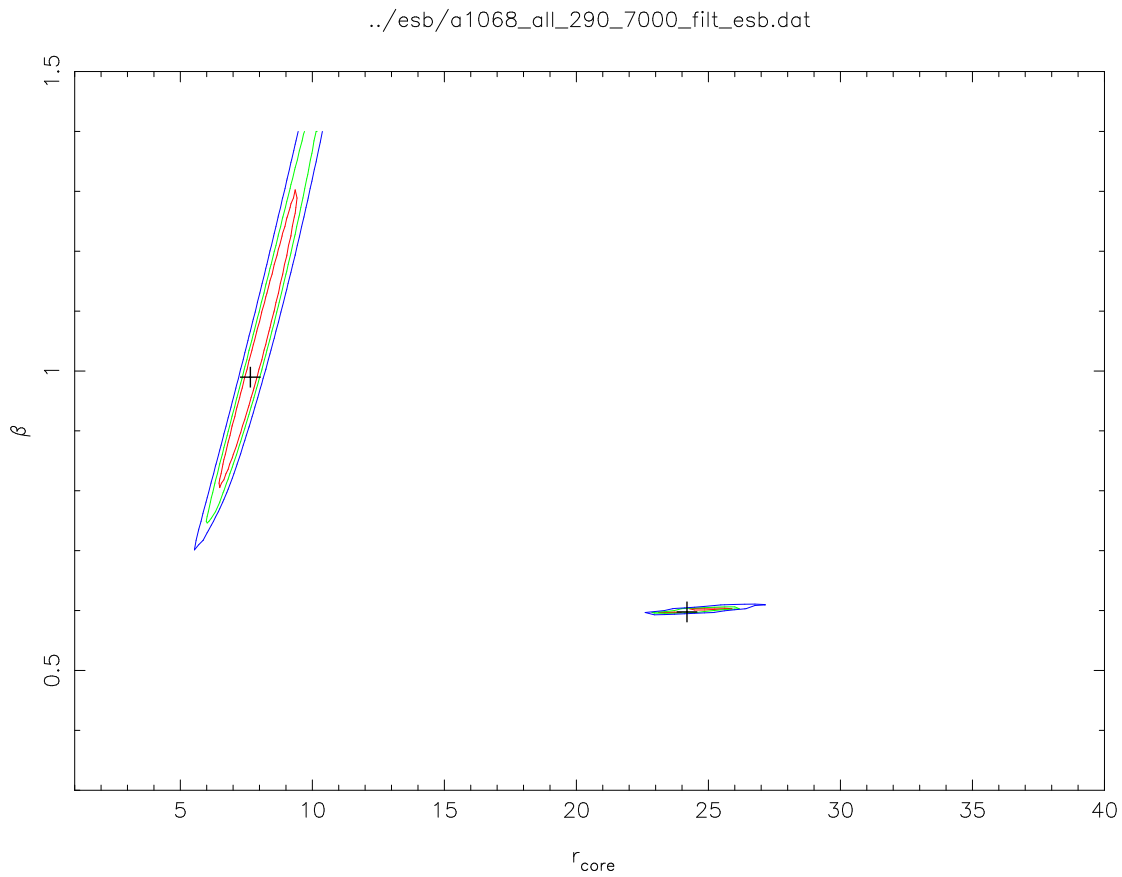


FIG. 11.— Confidence contours for the two components of the double  $\beta$  model fit to the surface brightness profile shown in Figure 10. Contours are shown for  $1\sigma$ ,  $2\sigma$ , and  $3\sigma$ . The crosses indicate the location of the best fit  $(r_c, \beta)$  values for the two components.

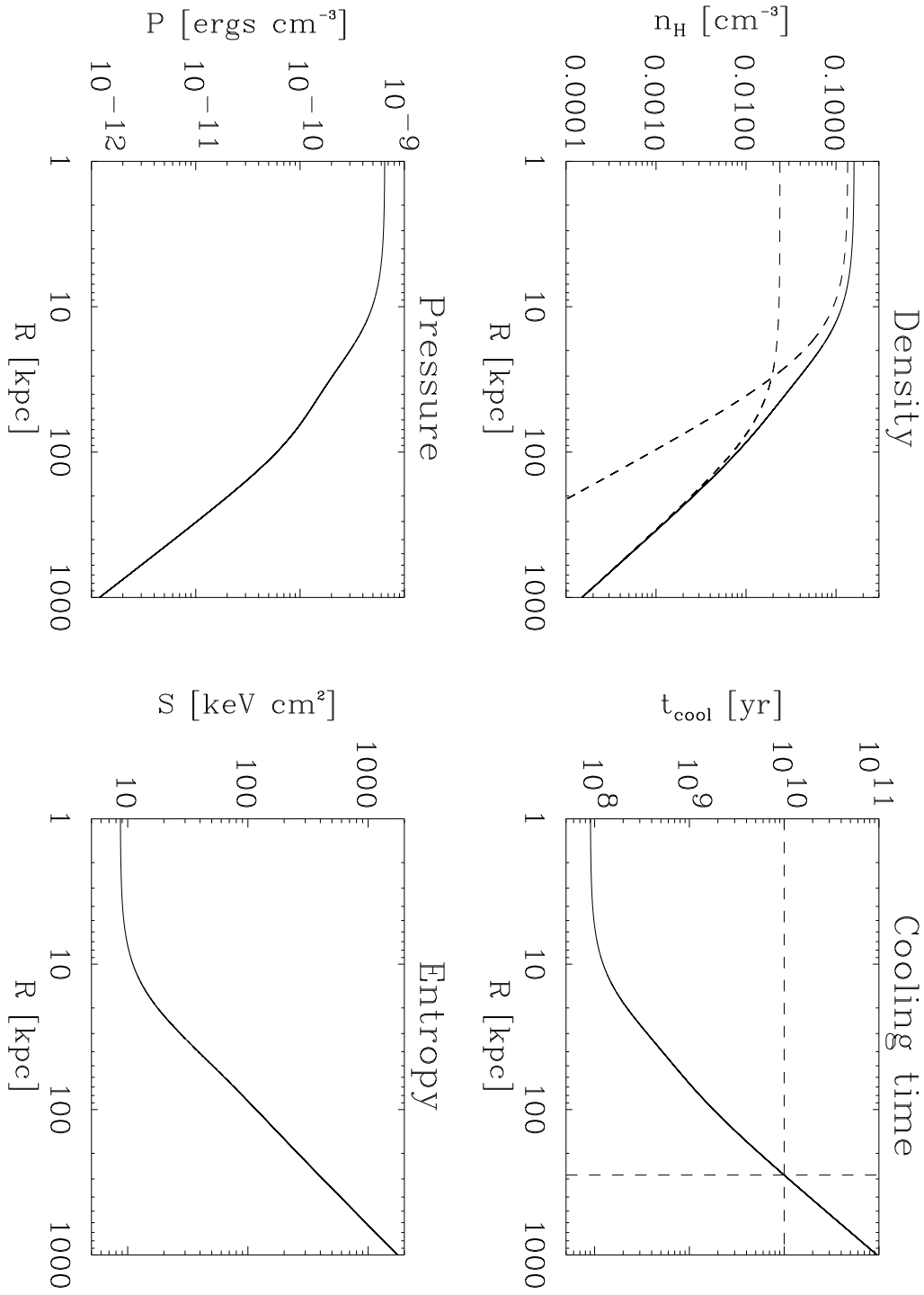


FIG. 12.— Radial variation of (a) electron density, (b) isobaric cooling time, (c) pressure, and (d) entropy. In panel (a), the dashed lines depict the two components of the electron density from the double  $\beta$  model fit to the surface brightness distribution. In panel (b), the horizontal line indicates a cooling time equal to  $10^{10}$  years and the vertical line indicates the corresponding cooling radius.

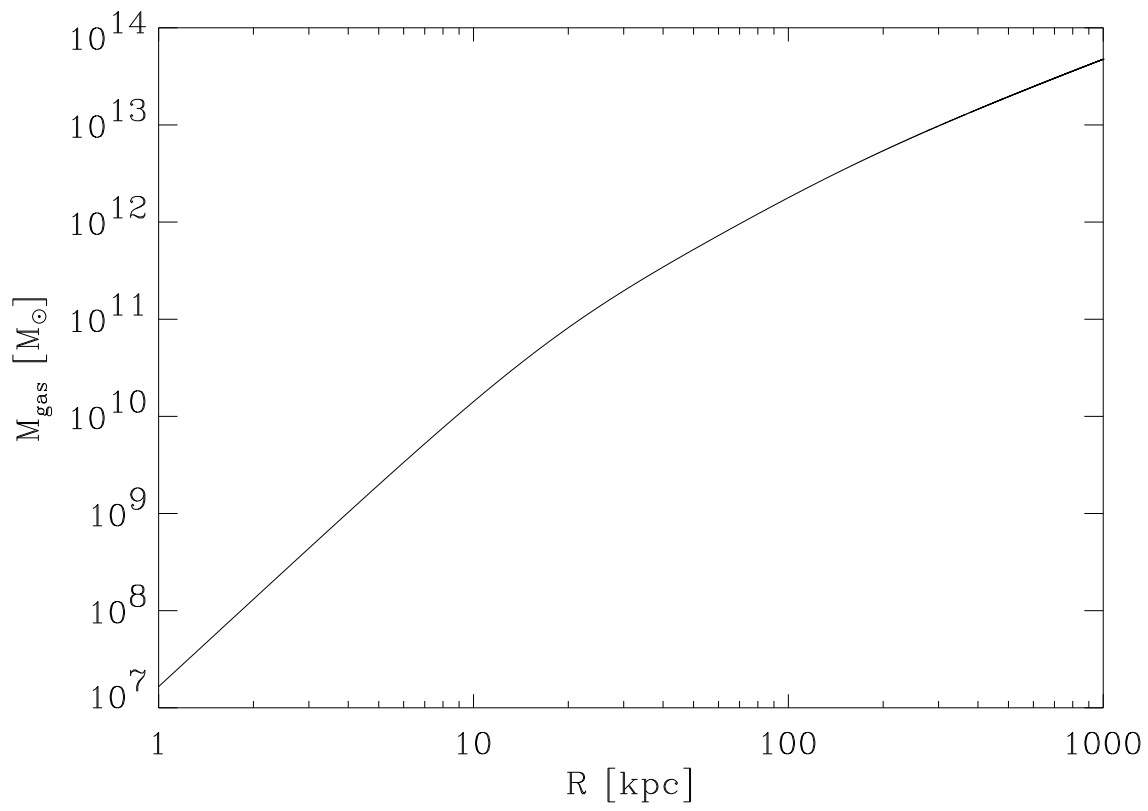


FIG. 13.— Gas mass profile for Abell 1068.



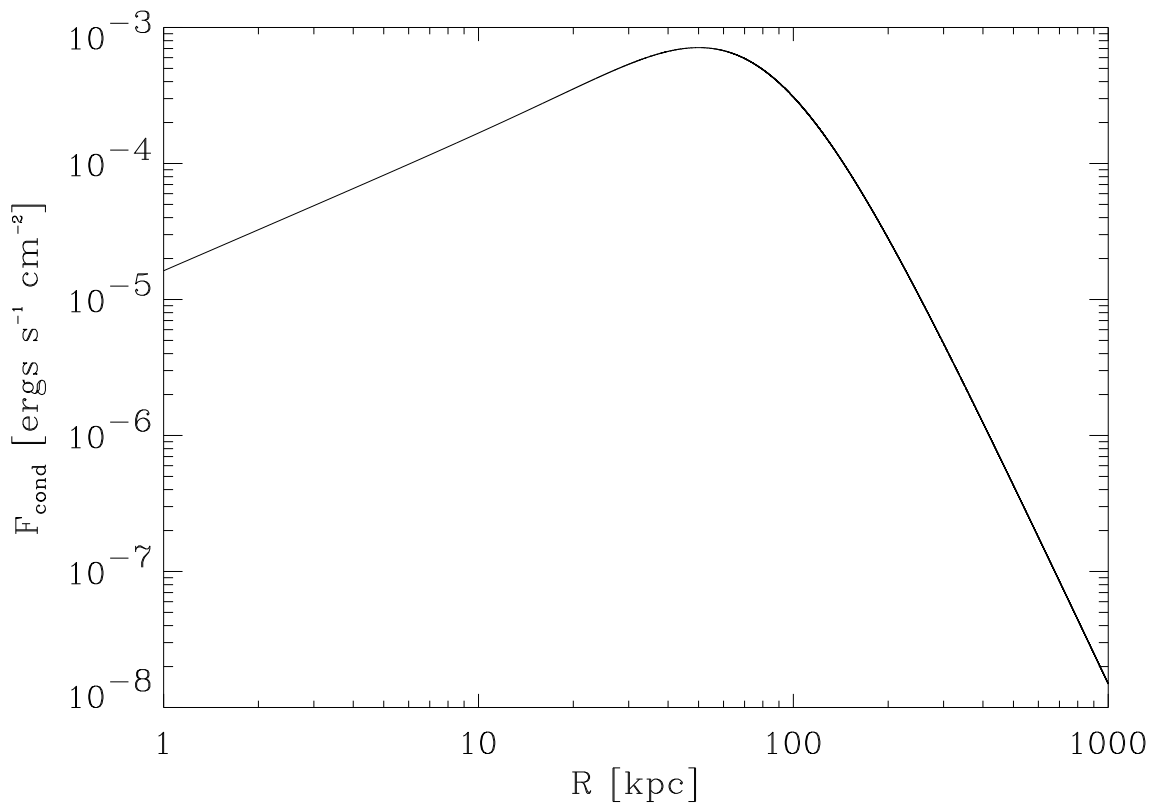


FIG. 14.— Heat flux due to thermal conduction as a function radius in the cluster assuming conduction operates at the Spitzer value (i.e.,  $\kappa = \kappa_{sp}$ ).

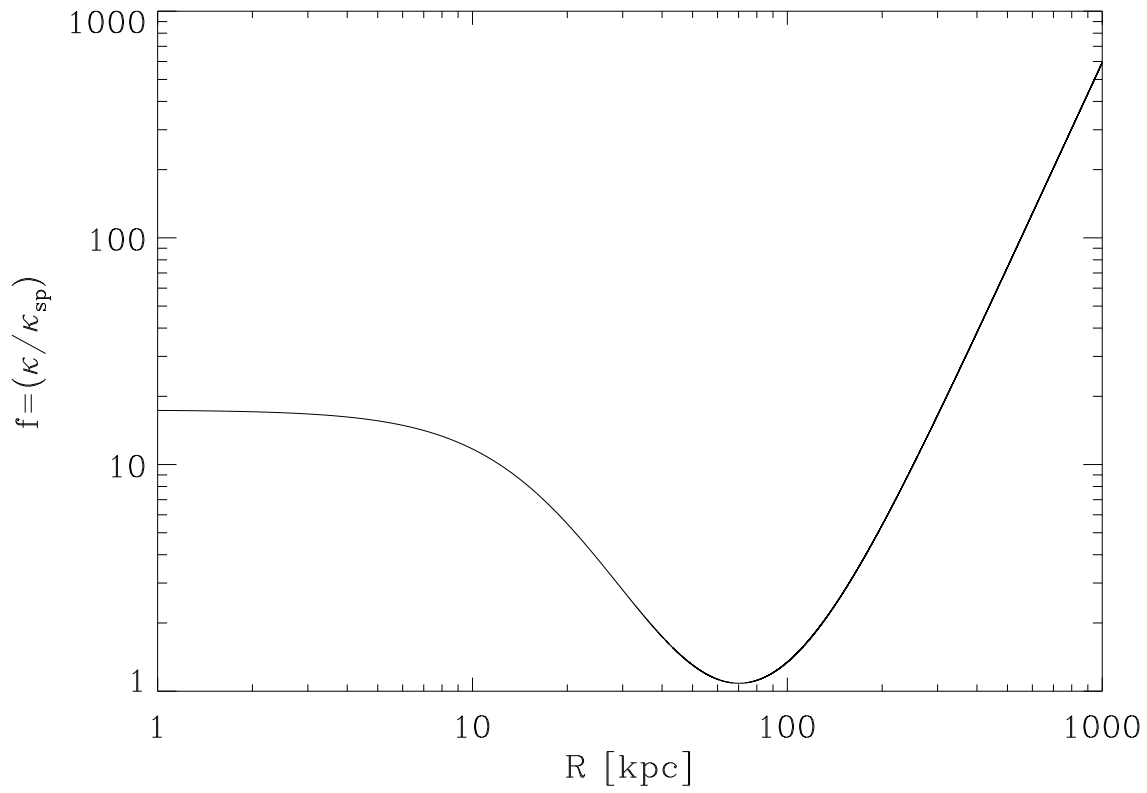


FIG. 15.— Value of the conduction parameter,  $f$ , required to balance radiative cooling as a function of radius in the cluster. The conduction parameter is expressed as a ratio relative to the Spitzer value.